Water quantification in silicate glasses by Raman spectroscopy: Correcting for the effects of confocality, density and ferric iron

Federica Schiavi, Nathalie Bolfan-Casanova, Anthony C. Withers, Etienne Médard, Mickaël Laumonier, Didier Laporte, Taya Flaherty, Alejandra Gómez-Ulla

Water quantification in silicate glasses by Raman spectroscopy: correcting for the effects of confocality, density and ferric iron

Federica Schiavi*[,1], Nathalie Bolfan-Casanova[1], Anthony C. Withers[2], Etienne Médard[1,3], Mickaël Laumonier[1], Didier Laporte[1], Taya Flaherty[1], Alejandra Gómez-Ulla[1]

[1]Université Clermont Auvergne, CNRS, IRD, OPGC, Laboratoire Magmas et Volcans, F-63000 Clermont-Ferrand, France

[2]Department of Earth Sciences and Centre for Planetary Science and Exploration, University of Western Ontario, 1151 Richmond Street, London, Ontario, Canada

[3]Universities Space Research Association, Lunar and Planetary Institute, Houston, TX, United States

*Corresponding author e-mail: f.schiavi@opgc.univ-bpclermont.fr

Abstract

New series of alumino-silicate glasses spanning a wide range of chemical compositions (basanites, tholeiitic basalts, calcalkaline andesites, peraluminous and peralkaline rhyolites) and with water contents from 0.02 to 6.70 wt % were used for improving the method of quantification of dissolved water with a highly confocal Raman micro-spectrometer. After reconsideration of previously proposed methods for spectra acquisition and post-analysis data treatment, we define the main critical steps that allow minimizing glass matrix effects. First, we carefully assess the variation of Raman band intensities, in both water (~ 3000-3800 cm^{-1}) and alumino-silicate vibration (~ 200-1250 cm^{-1}) regions with focus depth of the laser beam inside the sample. Our results indicate that in the first 2-10 μm depth, the intensity increase in the alumino-silicate region is twice as high as that in the water region. Optimal focus depths, where the signal of the water band is maximum and the intensity ratio of the water band to alumino-silicate band is minimum, vary with glass composition and confocal performance of the Raman spectrometer. This influences both external and internal calibration slopes. Second, this study recognizes critical parameters related with glass density, presence of ferric iron and dissolved carbonates as mainly responsible for matrix effects on the internal

calibration method. (a) We provide a procedure for correcting the effect of glass density on water internal calibration based on the observation that the integrated intensity (i.e. the area) of the alumino-silicate envelope generally drops with the increase of water content and decrease of glass density. (b) In CO_2-bearing glasses, the intensity of the ν_1 Raman vibration of dissolved carbonate at ~1087 cm^{-1} has to be subtracted from the intensity of the alumino-silicate envelope before applying the density correction. (c) Using peak-fitting, the intensity of the 850-1250 cm^{-1} envelope of peralkaline rhyolitic glasses is corrected for the effect of the presence of four-fold coordinated Fe^{3+}, as revealed by the strong Raman scattering of the vibrational mode at ~980 cm^{-1}. Following this procedure, all the studied glasses define a single calibration line in spite of their compositional variability, when using either of the two classical approaches referred to as *external* and *internal* calibration methods. The linear fits of the external and internal calibrations reproduce the whole dataset within 0.13-0.11 wt % (high and standard confocality) and 0.17 wt %, respectively. The accuracy of the external calibration is evaluated based upon comparison with ion-probe measurements of water dissolved in natural glass inclusions: the relative standard deviation is ~4% (1σ) on average, and reaches ~12% (1σ) for water contents of ~0.1 wt%.

Keywords: confocal Raman spectroscopy, water quantification, alumino-silicate glasses, glass density, peak fitting, glass inclusions

1. INTRODUCTION

Concentration, speciation and distribution of volatile species dissolved in silicate melts are key factors that control the physico-chemical evolution of magmas from their genesis to their final emplacement and affect the dynamics, style, and intensity of volcanic eruptions (e.g., Carroll and Holloway, 1994; Cashman 2004; Sanchez-Valle et al., 2015). Volatiles are

also important in mantle processes as they control melting and mantle rheology. Crucial information about volatile contents of magmas and behavior of volatiles at depth is usually recorded in small objects, such as phenocryst-hosted melt and fluid inclusions and tiny pockets of glassy matrix (e.g., Andersen and Neumann, 2001; Métrich and Wallace, 2008).

Raman spectroscopy is a useful micro-analytical technique for identification and quantification of volatiles contained in a variety of materials, which are of interest in volcanological and petrological studies, in particular water (regardless of speciation) dissolved in natural glasses. With respect to the other micro-analytical techniques used for quantification of water in rock samples, such as Fourier transform infrared spectroscopy (FTIR), secondary ion mass spectrometry (SIMS), and elastic recoil detection analysis (ERDA), Raman spectroscopy has several advantages: (i) it requires minimal sample preparation, (ii) it is non-destructive, (iii) it allows rapid analysis with high spatial resolution, which is of utmost importance for characterization of small samples and samples with small-scale heterogeneity, and (iv) it allows analysis of unexposed glass, fluid and solid inclusions contained in transparent minerals and interstitial glass pockets (e.g., Thomas, 2000; Thomas et al., 2006; Chabiron et al., 2004; Zajacz et al., 2005; Di Muro et al., 2006a; Severs et al., 2007; Frezzotti et al., 2012; Morizet et al., 2013; Freitas et al., 2017).

Since the work by Thomas (2000), several studies have shown that accurate quantification of water dissolved in natural glasses can be achieved after proper calibration of Raman spectrometers (Chabiron et al., 2004; Zajacz et al., 2005; Behrens et al., 2006; Di Muro et al., 2006a, 2006b; Thomas et al., 2006; Mercier et al., 2009, 2010; Le Losq et al., 2012; Di Genova et al., 2017). These studies investigated the advantages and limitations of distinct calibration methods. The first method is called “external calibration”, as quantification of water in the unknown sample is obtained by comparing the intensity (i.e. the

height, hereafter I_{OH}) or the integrated intensity (i.e. the area, hereafter A_{OH}) of the water band located around 3570 cm^{-1} (Fig. 1) with water band intensities or integrated intensities of well-characterized standard glasses. The relationship between intensity of the water Raman band and water concentration (hereafter referred to as "calibration curve") determined in these studies displays a slope that varies as a function of glass type. Dependence of the slope on glass composition is especially apparent when glasses belonging to alkaline and sub-alkaline series are compared (Behrens et al., 2006; Di Muro et al., 2006b; Mercier et al., 2010). According to Mercier et al. (2010), glass reflectance and density, as well as water environment, are the main parameters causing matrix effects on the external calibration. Thus, a set of glass standards spanning a wide range of compositions seems required for accurate quantification of water in natural glass samples.

The second calibration method is known as "internal calibration" because the intensity of the Raman water band is normalized to the intensity of bands located in the silicate region: either in the entire alumino-silicate region between 200 and 1250 cm^{-1} (Behrens et al., 2006; Le Losq et al., 2012; Di Genova et al., 2017), the band located at high wavenumbers between 850 and 1250 cm^{-1} (Zajacz et al., 2005; Behrens et al., 2006; Severs et al., 2007; Mercier et al., 2009), or the band at low wavenumbers ranging from 200 to 650 cm^{-1} (Thomas, 2000; Chabiron et al., 2004; Behrens et al., 2006; Mercier et al., 2009) (Fig. 1). Intensity versus content relationships obtained with an internal calibration procedure are expected to be less affected by instrumental and analytical conditions, such as laser power fluctuations, focusing errors, and differences in confocal volume size, light absorption and reflectance that depend on glass structure and composition. In reality, internal calibrations also depend on glass chemical composition, because both bands in the alumino-silicate region and the average Raman scattering cross section of all the different alumino-silicate structural units (Q^n) depend on glass composition (Franz and Mysen, 1995).

In order to correct the calibration of water concentration for compositional dependence, some authors have proposed additional normalization procedures taking into account the degree of glass polymerization (Zajacz et al., 2005; Mercier et al., 2010). Le Losq et al. (2012) defined a new protocol for spectra background subtraction that partly eliminates the effects of matrix composition. However, this method tends to overestimate and underestimate the water content of iron-poor and iron-rich samples, respectively (Di Genova et al., 2017). According to Di Genova et al. (2017), the use of different baseline procedures is not sufficient to remove the dependence of the internal calibration procedure on the iron content and oxidation state.

So far, there is no satisfactory methodology that allows quantifying the water content in glasses of variable composition using Raman spectroscopy. In this study, we reconsider previously proposed strategies for spectra acquisition and post-analysis data treatment, with the aim to establish the procedures under which a composition-independent calibration can be obtained when applying both external and internal calibration methods. For this purpose, we have studied glasses spanning a wide range of compositions belonging to both sub-alkaline and alkaline magma series. First, we investigate in detail how confocal performance and focus depth of the laser beam affect the calibration and highlight the importance of considering these parameters. Then, the effects of physico-chemical characteristics of alumino-silicate glasses, in particular those in relation to density and presence of ferric iron, are quantified, and we propose correction strategies to minimize matrix effects on the internal calibration. Finally, we test our method by analyzing natural glass inclusions of variable composition, whose water content was measured using SIMS or FTIR techniques.

2. METHODOLOGY

2.1 Starting materials

125 Thirty alumino-silicate glasses including basanites, tholeiitic basalts, calcalkaline
126 andesites, peraluminous and peralkaline rhyolites were used for calibration of water contents
127 by Raman spectroscopy (Table 1, Fig. 1S). Their polymerization degree (expressed as the
128 ratio of nonbridging oxygens per tetrahedrally coordinated cations, NBO/T) calculated on an
129 iron-free and H_2O-free basis varies from 0.0 to 0.78 (Table 2).

130 Two distinct sets of rhyolitic glasses were synthesized from the Güney Dag obsidian
131 (Turkey; Druitt et al., 1995) and from a peralkaline rhyolite (labeled as NSL) from New
132 Zealand, whose exact provenance is unknown (Behrens and Jantos, 2001) (Table 1). Both
133 rhyolites are very poor in microlites. The Güney Dag rhyolite is mildly peraluminous, SiO_2-
134 and Al_2O_3-rich (~77 and 12.5 wt %, respectively), FeO- and CaO-poor (0.8 and 0.25 wt %,
135 respectively) and contains 1.39 wt % H_2O (Mourtada-Bonnefoi and Laporte, 2002). This
136 relatively large H_2O content is due to the water contained in the glass phase of the obsidian
137 (1.05 ± 0.05 wt %; Mourtada-Bonnefoi and Laporte, 2002) and to the presence of biotite and
138 amphibole microlites (Cluzel et al., 2008). The rhyolite from New Zealand has lower SiO_2
139 (~75 wt %) and Al_2O_3 (~10 wt %), higher Fe (as total FeO ~4 wt %) and Na_2O (~5.5 wt %)
140 contents, and contains 0.1-0.4 wt % H_2O.

141 Two sets of basaltic glasses were synthesized starting from a primitive high-alumina
142 basalt erupted from the Giant Crater Lava Field (Medicine Lake volcano, California; Médard
143 and Grove, 2008; Malfait et al., 2011) and from tephra erupted from Holuhraun volcano
144 (Iceland) in 2014 (Haddadi, 2016). The composition of the Medicine Lake volcano basalt
145 (labeled as 82-72f) is very close to that of primitive mid-ocean ridge basalts, with a higher
146 Al_2O_3 content (~18.5 wt %). The composition of the basalt from Holuhraun is richer in FeO
147 (~12.5 wt %) and poorer in Al_2O_3 (~14 wt %) and is typical of lavas erupted from the
148 Bárðarbunga magmatic system (Sigmarsson and Halldorsson, 2015).

A set of reference glasses with basanitic composition and bearing different amounts of H_2O and CO_2 were synthesized from a natural basanitic tephra sampled at Thueyts volcano (Ardèche, France). The tephra composition is characterized by low SiO_2 (~45 wt %) and high total alkali (~6 wt %).

We also synthesized an intermediate (andesitic) composition closely reproducing the andesites erupted at Mt. Shasta (California, Grove et al., 2002) with a slight difference in Na_2O concentration. The details of the syntheses are presented below.

2.2 Experimental Procedures

The experimental work was carried out at the Laboratoire Magmas et Volcans (Clermont-Ferrand), except for the synthesis of glasses derived from the NSL and 82-72f starting materials. The synthesis of the 82-72f basaltic set is reported in Médard and Grove (2008) and is summarized in Table 1. Hydrous glasses were synthesized from the NSL rhyolitic obsidian using an internally heated pressure vessel at the Institut für Mineralogie of Hannover (Germany). The natural rhyolitic composition and double-distilled water were sealed in gold capsules and held at 1000 °C and 300-500 MPa for 72-120 h before quenching (for further details see Withers and Behrens, 1999).

For the synthesis of the andesitic glasses, we used a decarbonated mixture of oxide (SiO_2, TiO_2, Al_2O_3, FeO, MnO and MgO), silicate ($CaSiO_3$) and carbonate (Na_2CO_3, K_2CO_3) reagent powders. SiO_2, Al_2O_3, and MgO powders were dried in platinum crucibles in air at 1000-1100 °C overnight. $CaSiO_3$ and carbonate powders were dried in air at 250-400 °C overnight. These dried powders were weighed and ground altogether in an agate mortar to ensure a homogeneous starting mixture. For decarbonation and fusion, the mixture was held in a platinum crucible and heated by a gas-mixing furnace at one bar; as temperature changed, the gas mixture was adjusted to maintain fO_2 near FMQ buffering conditions. Temperature

was increased to 1000 °C in 6 hours, kept constant overnight, then increased and held for 30 min at 1400 °C before quenching the glass in water. In order to obtain a homogeneous glass, grinding and fusion were repeated a second time. Finally, the glass was ground for two more hours in an agate mortar to produce a very fine powder used in hydration experiments.

Cylinders of natural Güney Dag obsidian were drilled (4.5 mm in diameter, 4-5 mm in length) and cleaned with acetone in an ultrasonic bath. The Holuhraun basaltic tephra were crushed into small chips, carefully examined in order to remove possible crustal contaminants, and then ground in an agate mortar for ~ 2 hours. An analogous procedure was used for preparation of the starting powder with basanitic composition.

Anhydrous glasses were synthesized by re-melting the starting materials in a gas-mixing furnace at one bar, 1300 °C and fO_2 ~FMQ (Table 1). The starting materials were loaded into Au_{80}-Pd_{20} capsules whose upper side was left open to allow degassing, held at high temperature for several hours, and finally drop-quenched in water.

The hydrous glasses were synthesized in a piston-cylinder apparatus using a Pyrex-MgO assembly, a graphite heater, an outer NaCl cell, and Au_{80}-Pd_{20} capsules (5 and 4 mm outer diameter for 3/4" and 1/2" assemblies, 0.2 mm wall thickness, 4-5 mm length). First, deionized water was added at the bottom of the capsule using a micro-syringe; after loading and compacting ~100 mg of glass powders (or cylinders), the capsule was welded shut. We checked for leaks during capsule preparation by weighing the welded capsules before and after 1-hour heating at 120 °C in an oven. For the synthesis of H_2O and CO_2-bearing glasses with andesitic and basanitic compositions (Table 1), we added a mixture of water and oxalic acid dihydrate ($C_2H_2O_4 \cdot 2H_2O$) to glass powders. After welding, the capsules were placed in an oven first at 350 °C for 1 hour to decompose the oxalic acid, and then at 120 °C overnight to ensure homogenous distribution of the volatiles. In all experiments, the *P*-*T* conditions

were chosen to be well above the volatile saturation curve (Duan, 2014). The temperature was measured very close to the capsule by a $W_{95}Re_5$-$W_{74}Re_{26}$ thermocouple. Hydration experiments were ended by switching off the heating power, quenching the samples at cooling rate > 80 °C/s. Experimental conditions are reported in Table 1.

The glasses recovered from the experiments were cut and polished on one or both sides for major element characterization by electron microprobe and water and CO_2 concentration measurements by infrared and Raman spectroscopies. Homogeneity of the glasses was first checked under the microscope. All analyzed glasses were bubble- and crystal-free, except for one andesitic water-rich glass (A011215) that contains microlites crystallized upon quenching. The microlite-bearing glass is not suitable as standard; however, since the percentage of microlites is small and glass composition is homogeneous, it was used for comparison in Raman measurements.

2.3 Electron microprobe

Major element composition of glass samples was determined with a CAMECA SX100 electron microprobe (EMP) at the LMV. Glass analyses were performed with 15 kV accelerating voltage, 4-8 nA beam current, and a 20 µm (10 µm for basanitic glasses) defocused beam in order to reduce Na loss. The acquisition time was 20 s for Al (and for Mg and Ca in basanitic glasses) and 10 s for the other elements. Average major element compositions of the glasses are reported in Table 2. EMP measurements confirm compositional homogeneity of the studied glass samples.

2.4 Infrared Spectroscopy

Total water content of reference glasses was determined by Fourier Transform Infrared Spectroscopy, using a Bruker Vertex 70 spectrometer coupled with a Hyperion microscope system, housed at LMV. Spectra were recorded using a Globar light source, a KBr

beamsplitter and a MCT (Mercury-Cadmium-Tellurium alloy) detector. Plane parallel, double polished glass samples were placed on a CaF_2 window. Absorbance and background spectra of the glasses were obtained by acquisition of 300 and 100 scans, respectively. Beam size was 70 × 70 μm and spectral resolution was 4 cm^{-1}. Concentrations of OH groups and molecular H_2O were determined from the height of the absorbance bands at 4500 and 5240 cm^{-1}, respectively, using the Beer-Lambert law (e.g. Stolper, 1982). The 4500 and 5240 cm^{-1} bands are commonly assigned to a combination of the stretching vibrations of OH groups attached to Si and the combination of the stretching and bending vibrations of the H_2O molecule, respectively. Total water contents of the basaltic glasses belonging to the Holuhraun set, the basanitic glasses and two water-poor andesitic glasses (A030417 and A040417) were derived from the height of the broad asymmetric band at 3570 cm^{-1}, which contains the fundamental OH stretching vibrations of both molecular H_2O and Si-OH (and Al-OH) structural groups (e.g. Stolper, 1982). Baseline correction (see below) and peak integration were performed using OPUS software. On each sample, we carried out several measurements in order to verify compositional homogeneity. Homogeneity was confirmed by small relative standard deviations (RSD < 5 %) associated with water measurements on each sample.

Sample thickness was typically measured with a Mitutoyo digital gauge, except for very thin or small samples. In the latter case, we measured the sample thickness by reading the vertical displacement of the microscope stage between the top surface of the polished sample and the sample holder accurately determined when the Raman laser beam is focused. The accuracies of the two methods are ± 1 μm and < 1 μm, respectively. Thicknesses (and associated standard deviations) reported in Table 1 are average values of 4-8 measurements.

Glass density (ρ) was accurately measured with a microbalance using Archimedes' method and deionized water as the immersion liquid. Two to six repeated measurements on

each glass sample gave reproducibility better than 2 % relative. Densities of the studied reference glasses are reported in Table 1 and Figure 2.

The largest uncertainty in water contents determined by FTIR analysis is due to the uncertainty on the molar absorptivity (i.e. extinction coefficient) for the absorbance bands at 4500 and 5240 cm^{-1}. As estimated absorptivity coefficients depend on the baseline subtraction method (e.g. Ohlhorst et al., 2001), we followed guidelines provided by Ohlhorst et al. (2001) and Mandeville et al. (2002) for proper choice of baseline fitting procedure and molar absorptivity values.

In rhyolitic glass spectra, a linear baseline was fitted as tangent through the minima on both sides of the 5240 cm^{-1} band and then extrapolated below the 4500 cm^{-1} band (GG baseline of Withers and Behrens, 1999). For peraluminous rhyolites, we used the absorption coefficients provided by Withers and Behrens (1999): 1.52 ± 0.08 L mol^{-1} cm^{-1} for ε_{4500} (OH) and 1.72 ± 0.06 L mol^{-1} cm^{-1} for ε_{5240} (H_2O). Measured water concentrations in rhyolitic glasses match with target compositions (i.e. the amount of water loaded into the capsule) and are close to the difference of EMP analyses total from 100 wt %.

For andesitic glasses, we used the average values of the extinction coefficients determined by King et al. (2002) and Mandeville et al. (2002): 0.97 L mol^{-1} cm^{-1} for ε_{4500} (OH), 1.08 L mol^{-1} cm^{-1} for ε_{5240} (H_2O), and 66.32 L mol^{-1} cm^{-1} for ε_{3570} (total water). Mandeville et al. (2002) showed that ε_{4500} and ε_{5240} molar absorptivities have significant compositional dependency and can be predicted if the tetrahedral (Si^{4+}, Al^{3+}) cation /total cation fraction of the glass is known. Molar absorptivity values calculated for the andesitic glasses using the regression line equations provided by Mandeville et al. (2002) are ~ 1.00 and 1.19 (L mol^{-1} cm^{-1}) for ε_{4500} and ε_{5240}, respectively, which are very close to the adopted values. The baseline of andesitic glass spectra was fitted as tangent through three points: the minima on both sides of the 4500 cm^{-1} band and the minimum on the low wavenumber side of

the 5240 cm^{-1} band. On its high wavenumber side (at ~ 5400 cm^{-1}), the linear baseline intersects the absorbance curve. This baseline fitting procedure is analogous to the one performed by Mandeville et al. (2002). Measured water concentrations in andesitic glasses are slightly lower than target amounts loaded into the capsule due to minor loss either during capsule preparation or upon the synthesis experiments.

We determined water contents in the basanitic and Holuhraun basaltic glasses based on the height of the absorbance band at ~3570 cm^{-1}. This choice was driven by the observation that the spectrum background around the 4500 and 5240 cm^{-1} bands is strongly affected by the absorption of near infrared and visible electronic transitions or crystal field bands of iron (Ohlhorst et al., 2001). Consequently, baseline fitting around these bands becomes more laborious and the choice of ε_{4500} and ε_{5240} for basanites and iron-rich basalts may be less accurate. In contrast, the linear baseline under the large band at 3570 cm^{-1} is unambiguously defined. For basanites, we used the molar absorption coefficient provided by Shishkina et al. (2014), 57.3 ± 1.8 L mol^{-1} cm^{-1}. For basalts, we adopted the molar absorption coefficient provided by Mercier et al. (2010), 62.8 ± 0.8 L mol^{-1} cm^{-1}, which is very close to the coefficient measured by Dixon et al. (1995).

Carbon dioxide concentrations in four basanitic and two andesitic glasses were determined from the heights of the absorbance bands at 1430 and 1520 cm^{-1}, which correspond to antisymmetric stretching of distorted carbonate groups (Dixon et al., 1995). For basanitic and andesitic glasses, we adopted respectively the molar absorption coefficients provided by Shishkina et al. (2014) (306 ± 32 L mol^{-1} cm^{-1} for 1430 and 349 ± 25 L mol^{-1} cm^{-1} for 1520) and those given by King et al. (2002) (269 and 271 L mol^{-1} cm^{-1} for the 1430 and 1520 bands, respectively).

Water and CO_2 contents of a few andesitic and basanitic samples measured both by FTIR and elemental analyzer (Flash 2000 CHNS Thermo Electron housed at LMV) match within 5 %.

2.5 Raman Spectroscopy

Raman spectra were collected at LMV using an InVia confocal Raman micro-spectrometer manufactured by Renishaw and equipped with a 532 nm diode laser (200 mW output power), a Peltier-cooled CCD detector of 1024 x 256 pixels, a motorized XY stage and a Leica DM 2500M optical microscope. Scattered light was collected by a back-scattered geometry. An edge filter effectively reduced both Rayleigh scattered photons and photons from the exciting laser source at 0 cm^{-1} that had been reflected by the sample surface.

Laser power on the sample was reduced by filters in order to operate at three different powers of ~1, 8 and 16 mW. Laser power on the sample was periodically checked. A 2400 grooves/mm grating was used for the analyses, which resulted in a spectral resolution better than 1 cm^{-1}. A 100x microscope objective (numerical aperture 0.9) was used and the slit aperture was set to 65 μm (standard confocality setting) or 20 μm (high confocality setting). These analytical conditions result in lateral and axial spatial resolutions of ~1 and 2-3 μm, respectively, near the sample surface. Daily calibration of the spectrometer was performed based on a Si 520.5 ± 0.5 cm^{-1} peak. The 82-72f#9 basaltic glass was used as internal standard and analyzed several times during each analytical session in order to correct for the dependence of band intensities on delivered energy. The spectra were recorded from ~100 to 1350 cm^{-1} (alumino-silicate network domain) and from ~2900 to 3800 cm^{-1} (water domain) Raman shifts using Wire 4.2 software. Acquisition times were set to 120-180 s and 120-600 s for the alumino-silicate and water domains, respectively. The longest acquisition was adopted for analysis of water-poor glasses at 1 mW laser power, in order to obtain high signal-to-noise ratios. Under these operating conditions, no melting or water loss was detected. However, we

observed that the Raman signal intensity of the dark H_2O- and Fe-rich basalt from the Holuhraun set was unstable at the highest laser power we used, possibly due to glass heating by the laser beam.

The lower limit of water detection using the analytical conditions detailed above was measured in olivine-hosted melt inclusions from FAMOUS Zone (Mid-Atlantic Ridge; Schiavi et al., 2016) and was slightly lower than 0.1 wt %.

Analytical precision calculated based on repeated daily measurements of reference glasses is generally better than 6 % and 2 % relative, respectively, in water-poor and water-rich glasses in highly confocal setting. This difference is mainly related to degradation of the signal-to-noise ratio in spectra of water-poor glasses. Performing measurements under standard confocality conditions yields better analytical precision because the analyzed volume is larger, so Raman signal is more intense and small differences in focusing depth are less critical. We observed that reproducibility decreases for measurements performed on the sample surface, especially for laser powers < 10 mW. When the laser beam is focused on the sample surface, in fact, small variations of the excited sample volume are more likely to occur because the beam is not entirely inside the sample and reflectance at the sample surface has a more important effect.

In this study, reference glasses for Raman spectroscopy analysis were prepared as large free chips (i.e. not embedded in epoxy resin or other embedding medium). We verified the homogeneity of the reference glasses by acquiring several spectra on each glass during the same analytical session. In addition, repeated measurements confirmed that no water loss occurred over several months. In A011215, presence of microlites was not detected most likely due to wide spacing between microlites relative to the diameter of the analysis spot.

3. GLASS DENSITY

Figure 2 shows the relationship between glass densities, ρ (kg/m^3), and water contents, C_{H2O} (wt %), determined by FTIR spectroscopy or SIMS (Table 1). A linear relationship $\rho = \rho_0 + b\ C_{H2O}$, where ρ_0 is the density of the anhydrous glass and b the slope of the line, is observed. Density diminishes with increasing water content. The slope for mafic glasses is more important than the ones for intermediate and felsic glasses. The slopes defined by the rhyolitic and andesitic sample sets are in agreement with those found by Ohlhorst et al. (2001) and Behrens et al. (2006) for similar glass compositions. Moreover, the measured rhyolitic and andesitic glass densities are very close to densities measured by Withers and Behrens (1999) and Mandeville et al. (2002). The slope obtained for the 82-72f basaltic set is slightly more pronounced than the slope reported by Ohlhorst et al. (2001) for basaltic composition. As expected, the Fe-richer sets of basaltic and rhyolitic glasses are characterized by higher densities than the Fe-poorer sets. The measured basanitic glass densities fall within the range of values calculated by Iacovino et al. (2016). Density of the A011215 sample is aligned with that of the other andesitic glasses, even though it contains microlites.

4. RAMAN SPECTRAL TREATMENT

4.1 Baseline fitting

Raman spectra of glass samples required baseline correction before being used for quantification of volatile species. In fact, a high signal intensity characterizes glass spectra at low wavenumbers (i.e. small Raman shifts, Fig. 3) due to the influence of the intense Rayleigh diffusion tail superimposed by the boson peak (e.g. Le Losq et al., 2012). Long (1977) was the first to highlight the need for correcting the raw spectra for the dependence of Raman scattering on frequency and temperature. Glasses, in particular rhyolitic ones, can be affected by fluorescence, which modifies the shape and intensity of the spectrum background.

Moreover, the slope of the background is influenced by the total glass iron and oxidation degree (Di Muro et al., 2009). As spectrum topology strongly depends on glass composition and degree of polymerization, baseline correction is a critical step in the treatment of Raman spectra, especially in the alumino-silicate vibration region (Figs. 3 and 4). On the other hand, the baseline subtraction procedure does not affect significantly the treatment of the total water band around 3570 cm^{-1}.

In previous studies, different approaches were adopted for defining the baseline shape and the choice of anchor points (e.g., Zajacz et al., 2005; Behrens et al., 2006; Severs et al., 2007; Di Muro et al., 2009; Mercier et al., 2009, 2010; Le Losq et al., 2012). A first approach consisted in fitting the baseline of raw spectra using either a combination of linear baselines (Severs et al., 2007), a cubic baseline (Mercier et al., 2009) or a cubic spline baseline (Behrens et al., 2006) with three/four anchor points in the alumino-silicate vibration region and two anchor points in the water domain (Fig. 1). Zajacz et al. (2005) used a linear extrapolation of the flat signal from the 1250–1850 cm^{-1} spectral region towards low wavenumbers (Fig. 1). Such an extrapolation is possible only if the spectral background between 1250 and 1850 cm^{-1} is not too steep. In a second approach, the baseline was subtracted from spectra that had been previously corrected for Long's correction (Long, 1977). Behrens et al. (2006) and Di Muro et al. (2009) adopted, respectively, a cubic spline and a cubic baseline anchored only at the extremities of the alumino-silicate and water domains, whereas Le Losq et al. (2012) anchored the spline to a limited number of intermediate minima. In general, we observe that discrepancies between different spectral corrections arise from unconstrained concavity of the spline baseline.

Difficulties are encountered in fitting the baseline in the alumino-silicate vibration region, because there is no simple *a priori* way to relate the shape of broad Raman bands to specific network vibrations and structures, although statistical analysis and peak fitting

391 algorithms provided interesting results in this direction (e.g., Herzog and Zakaznova-Herzog,
392 2011; Woelffel et al., 2015). Moreover, overlapping of bending and stretching bands occurs in
393 the alumino-silicate region (e.g. Mysen et al., 1980), resulting in substantial uncertainty in
394 selecting physically meaningful anchor points. The observed minima between the bands, in
395 fact, may include contributions of the vibration bands (e.g. Le Losq et al., 2012).

396 For baseline correction and subsequent peak integration, we used PeakFit package
397 software (Jandel Scientific). We used several procedures based on subtraction of linear (more
398 often a sequence of linear segments) and cubic baselines from raw spectra or Long-corrected
399 data (Fig. 3). Choice of anchor points for definition of linear and cubic baselines was dictated
400 by two requirements (Le Losq et al., 2012): 1) making our procedure simple and reproducible,
401 2) minimizing the arbitrariness due to operators' choices. In the alumino-silicate network
402 domain, we first fixed the anchor points at the two extremities of the spectrum where no
403 Raman signal occurs. In the case of linear baselines, these are tangent points to the curve (Fig.
404 3), whereas a wider range of points on the background was selected for cubic baselines. So,
405 anchor points at the two extremities were fixed at 340-360 and 1190-1200 cm^{-1} in basanitic
406 glass spectra, at 300-340 and 1200-1220 cm^{-1} in basaltic glass spectra, at 230-250 and 1230-
407 1250 cm^{-1} in andesitic glass spectra, and 190-210 and 1250-1260 cm^{-1} in rhyolitic glass
408 spectra. For cubic baselines, the background at the high frequencies was extended up to 1350
409 cm^{-1}. Then, a minimal number of intermediate anchor points were set in order to: a) prevent
410 linear baselines from crossing the spectrum, especially in rhyolites, andesites and basalts
411 spectra, and b) minimize the influence of the background characterized by different slopes at
412 the low frequencies, especially in basanites spectra (Fig. 3). For these reasons, an intermediate
413 anchor point was placed near 630 and 640 cm^{-1} in basanitic and basaltic glasses, and in the
414 645-700 and 670-710 cm^{-1} ranges in andesitic and rhyolitic glasses, respectively. Around the
415 minimum at 670-710 cm^{-1} of rhyolitic spectra, linear baselines resemble cubic baselines, as

several short linear segments are necessary to fit the curve. A second intermediate anchor point was set around 800-830 cm^{-1} in basalts, 825-840 cm^{-1} in andesites, and ~840 cm^{-1} in rhyolites. We did not fix an anchor near 820 cm^{-1} in basanites because the corresponding minimum tends to disappear in H_2O and CO_2-bearing basanites. The defined anchors correspond to minima regions, and in some cases are defined by tangent lines to the spectra. We note that the positions of the intermediate anchor points and that of the anchor at the high wavenumber end of the spectrum shift to higher frequency as the polymerization increases, in agreement with previous observations (Le Losq et al., 2012).

In the water domain of the spectra, linear baselines were anchored (~2980 and 3780 cm^{-1}) and cubic baselines were fit (from 2980 to 3000-3008 and from 3725 to 3780 cm^{-1}) at both band extremities without any distinction between glasses of different composition. As the shape of cubic baseline is more sensitive to the topology and length of the fitted background, the more adequate cubic fitting was considered the one with the closest match of the baseline on the background on both sides of the band.

4.2 Alumino-silicate band topology and assignment

4.2.1 Topology of Raman spectra

In the alumino-silicate region of the Raman spectrum (200 to 1250 cm^{-1}), glass samples typically show two main broad bands. The position of the bands and their topology, i.e. relative band intensities, band shape and FWHM (full width at half maximum), vary from one sample to another (Fig. 4), as they depend on glass structure, chemical composition and oxidation state. Note that the spectral features detailed in the following section are scarcely affected by the chosen method for baseline correction.

In basanitic and basaltic glasses, the most intense band occurs at higher frequency than the less intense one (Fig. 4). Following previous studies (Mercier et al., 2009), we label these

bands as High-Frequency (HF) and Low-Frequency (LF) bands. Increasing water content in basanitic and basaltic glasses has several effects: a) the maximum peak position of the LF bands shifts from 556 to 510 cm^{-1} and from 532 to 512 cm^{-1} in basanites and basalts, respectively; b) the maximum peak position of the HF bands shifts from 968 to 975 cm^{-1} in basanites, and from 966 to 990 cm^{-1} in basalts. c) The FWHM of the HF band slightly decreases from 181 to 164 cm^{-1} and from 184 to 177 cm^{-1} in the Fe-rich (Holuhruan) and high-Al (82-72f) basaltic sets, respectively (Fig. 2S b). d) In basalts, the ratio of LF band (integrated) intensity to HF band (integrated) intensity increases due to apparent decrease of the HF band height (Fig. 2S d). The latter observation is in agreement with previous observations on different basaltic glasses (Mercier et al., 2009). A shoulder at ~580 cm^{-1} characterizes the LF bands. A broad weak band centered at ~710 cm^{-1} defines the spectrum topology in the intermediate wavenumber range (650-800 cm^{-1}). In basanites, the relative intensity of this middle-region band with respect to LF and HF bands is higher than in the other glasses, and increases with the volatile content. Dissolved CO_3^{2-} molecules in basanites produce a peak near 1083 cm^{-1}, whose intensity increases with the CO_2 content, in agreement with Morizet et al. (2013).

With increasing polymerization, the relative intensity of the two main silicate bands inverts and the LF and HF maximum peaks shift, respectively, to lower and higher frequencies, in agreement with previous studies (e.g., Matson et al., 1983; Mercier et al., 2009). Moreover, the FWHM of the LF band diminishes with increasing degree of polymerization (Figs. 2S e,i).

In andesitic glasses, the maximum peak of the LF band occurs at 488 ± 3 cm^{-1}. The broader HF band is centered at ~1013-1022 cm^{-1} (with the only exception of the A071215 glass whose maximum peak is at 970 cm^{-1}). The ratio of LF band (integrated) intensity to HF

band (integrated) intensity increases with increasing degree of polymerization (Fig. 2S g). With increasing water content, the FWHM of the LF band decreases from 137 to 114 cm^{-1} (Fig. 2S f). As in basalts, the LF band exhibits a shoulder at ~580 cm^{-1}. A small asymmetric band centered at 795 cm^{-1} is present in all andesitic glasses (Fig. 4). Dissolved CO_3^{2-} molecules in A310317 and A030417 glass samples produce a peak near 1078 cm^{-1}, which is more pronounced in A310317.

Rhyolitic glasses are characterized by a main asymmetric band centered at 467-484 cm^{-1}. Maximum LF peak position shifts to higher frequency with increase of water content dissolved in the glass, contrary to what is observed in basalts. Its FWHM varies from 122 to 130 cm^{-1} and from 134 to 145 cm^{-1} in the peraluminous (Güney Dag obsidian) and peralkaline (NSL obsidian) glass sets, respectively; there is a negative correlation between FWHM and water content (Fig. 2S j), as pointed in andesitic glasses. In the peraluminous rhyolites, the LF band has a shoulder at ~580 cm^{-1}. A small band centered at 795 cm^{-1} is present in all rhyolitic spectra; its intensity slightly decreases with increased water content of peraluminous glasses. Major differences between the two glass sets and within each set are principally observed in the high wavenumber range (850 to 1200 cm^{-1}). In this range, the spectra are defined by several sub-bands, whose position, shape and relative intensities are strongly affected by glass composition and degree of polymerization (Fig. 4). Peraluminous rhyolites spectra show a less intense band centered at ~930 cm^{-1} and a more intense band centered at ~1135 cm^{-1}. The intensity of the band near 930 cm^{-1} slightly increases with water content. In the peralkaline rhyolites, instead, the band occurring at 1135 cm^{-1} is much smaller than the band located around 980 cm^{-1}. Compared to the glasses of the same set, the water-poor NSL-N1 glass differs in that its spectrum has a more pronounced band near 1050 cm^{-1}.

4.2.2 Review of the interpretation of bands

In the 200-1300 cm^{-1} region of the Raman spectrum, bands correspond to different bridging and non-bridging T-O vibrations in the glass structure (e.g., Brawer and White, 1977; Matson et al., 1983; McMillan, 1984; McMillan et al., 1992). The LF band near 400-500 cm^{-1}, which is dominant in polymerized glasses, is traditionally assigned to: a) rocking motion in fully polymerized Q^4 units (where Q^4 denotes a tetrahedron linked by bridging O atoms to 4 adjacent tetrahedra), b) breathing modes of four- and six-membered rings of TO_4 tetrahedra in polymerized glasses (Sharma et al., 1981; Matson et al., 1983; Rossano and Mysen, 2012), but also c) T-O-T symmetric stretching vibrations involving bridging oxygens and four-fold coordinated cations (Zotov et al., 1992) and d) T-O-T bending vibrations in glasses containing non-bridging oxygens (McMillan, 1984; Rossano and Mysen, 2012 and references therein). In rhyolitic glasses, decreasing FWHM of the LF band (Fig. 2S j) and its shift to higher frequency with increasing water content have been explained by a possible decrease in the average T-O-T angle (McMillan and Remmele, 1986).

The vibrational mode at 570-580 cm^{-1} has been attributed to either structural defects (i.e. broken oxygen bridges, Stolen and Walrafen, 1976; Seifert et al., 1981; McMillan and Remmele, 1986) or a mixed stretch-bend vibration in Q^2 structural units (Furukawa et al. 1981). The bands near 700 and 800 cm^{-1} have been respectively ascribed to T-O-T bending motions (Mysen et al., 1980; Furukawa et al. 1981; McMillan, 1984; Rossano and Mysen, 2012) and to cage-like vibrations of Si atoms mainly in Q^4 tetrahedra (Zotov and Keppler, 1998).

The main HF envelope at 900-1200 cm^{-1} can be decomposed into several bands associated with localized symmetric and asymmetric T-O and T-O-T stretching modes of distinct structural species, i.e. Q^2, Q^3, Q^4 (2, 3, 4 being the number of bridging oxygens; Mysen et al., 1980; Matson et al., 1983; McMillan 1984; Zotov and Keppler, 1998; Rossano and Mysen, 2012). Substitution of Al^{3+} and Fe^{3+} for Si^{4+} as network-forming cations strongly

513 influences the spectral composition of this band; in particular, increasing the Al content of the
514 glass results in the shifting of Raman bands to lower frequencies (Brawer and White, 1977;
515 Mysen et al., 1980; Neuville et al., 2004). The intensity ratio between the bands near 950 and
516 1135 cm^{-1} in rhyolitic glasses is indicative of relative proportions of structural units, which are
517 likely Q^2 and a combination of Q^3 and Q^4 units, respectively (Mysen et al., 1980; Zotov and
518 Keppler, 1998). The band near 1050 cm^{-1} that characterizes the water-poor NSL-N1 glass is
519 tentatively assigned to T-O stretching vibrations in distinct Q^3 or Q^4 units (Mysen et al., 1980;
520 Zotov and Keppler, 1998). In the peraluminous rhyolites, the increased intensity of the band
521 at ~930 cm^{-1} with increasing water content can be attributed to the formation of T-OH units
522 (Zotov and Keppler, 1998). In peralkaline glasses, the sharp increase of the band at 970-980
523 cm^{-1} is attributed to progressive entry of four-fold Fe^{3+} in alkali-bonded Q^3 units (Wang et al.,
524 1995; Di Muro et al., 2009; Di Genova et al., 2016).

525 The cause of the HF band shift of the andesitic glass A071215 to lower wavenumber
526 compared to the other andesitic glasses is uncertain: it is probably related to differences in
527 their Fe^{3+}/Fe_{tot} ratios.

528 In basaltic glasses, the increased intensity of the HF envelope and its shift to lower
529 wavenumbers compared to polymerized glasses are consistent with the increase of Q^2 and Q^3
530 units. In the high-Al basaltic set, both water content and polymerization degree correlate
531 negatively with the FWHM of the HF band (Fig. 2S a, b) and positively with the intensity
532 ratio of LF band to HF band (Fig. 2S c, d). This seems to be contradictory as water dissolution
533 is expected to enhance depolymerization. Although investigation of dissolution mechanisms
534 of water in basaltic melts is beyond the scope of this study, it is worth noting that the
535 described spectral features likely suggest dissolution mechanisms other than those occurring
536 in more polymerized glasses. In depolymerized CaO-MgO-SiO_2 glasses, Xue and Kanzaki
537 (2004) highlighted formation of (Ca,Mg)-OH groups, in which OH groups are only linked to

network-modifying metal cations, not to the silicate network. This is expected to cause an increase in the melt polymerization, contrary to the effect of Si-OH formation (Mysen and Virgo, 1986; Xue and Kanzaki, 2004). These water dissolution mechanisms, associated with major changes in the local environment of metal cations, are probably responsible for the trends defined by the high-Al basaltic set.

4.3 Water band topology

The topology of the water stretching vibration band depends on glass matrix composition and water concentration (Fig. 5), but also on water speciation (e.g., Mysen and Virgo, 1986) and strength of H-bonding (e.g., Zajacz et al., 2005; Behrens et al., 2006; Di Muro et al., 2006). Different water species (metal-hydroxyl and molecular H_2O) contribute to the intensity of the broad water band-envelope (e.g., Mysen and Virgo, 1986). The latter is asymmetric in shape with a long tail on the lower wavenumber side, and is characterized by two shoulders near 3250 cm^{-1} and 3640 cm^{-1} that are readily observed in rhyolitic glasses (Fig. 5). The exact position of the maximum peak of the water band shifts to lower frequency with increase of polymerization degree and water content (Fig. 5), in agreement with previous studies. The maximum is located within the 3565-3582 cm^{-1} range in basaltic glasses and at 3552-3570 cm^{-1} in basanitic, andesitic and rhyolitic glasses. In the basanitic, basaltic and andesitic glass sets, the FWHM of the band increases by 15-25 % relative with increasing water content.

The H_2O bending vibration at ca. 1630 cm^{-1} (not shown) can be clearly distinguished from the background in spectra of water-rich glasses.

4.4 Peak fitting of the HF and water bands

We performed spectral deconvolution using OriginPro software in order to quantify differences in spectral components of the water band and the HF alumino-silicate envelope of

basanitic and rhyolitic glasses (Tables 1S, 2S and 3S). Spectra were fitted with a finite number of Gaussian components using the Multiple Peak Fit tool and following a procedure analogous to the one described by Morizet et al. (2013). This procedure consists of: i) locating a certain number of peaks based on results of previous studies (e.g., Di Muro et al., 2009; Rossano and Mysen, 2012; Morizet et al., 2013); ii) performing a first set of iterations with peak position and/or FWHM fixed until the quality of fit (expressed as χ^2) does not change; and iii) performing a second set of iterations in which peak position and areas are left free to evolve, until the best fit possible (i.e., the lowest χ^2) is obtained. Fitting parameters were iterated until the fit converged using both Simplex method and Levenberg-Marquardt algorithm available in OriginPro, and the two algorithms provided comparable results. In our simulations, the χ^2 tolerance value of 10^{-9} was always reached. The errors associated with the simulations are reported in Tables 1S, 2S and 3S. The proposed simulations may represent one of several possible fits; however, consistency in fitting parameters within each glass series and general agreement with deconvolutions reported in the literature (e.g., Di Muro et al., 2009; Rossano and Mysen, 2012; Morizet et al., 2013) ensure the reproducibility of the calibrations established in the next sections. In fact, we verified that the small changes in the constrained parameters had a negligible effect on the ratios between the areas of different spectral components.

Five components are required to fit the spectra of rhyolitic glasses (Fig. 6). Peak fitting of peraluminous and peralkaline glass spectra differs in the position of component II and in the relative intensities of the five components (Table 1S). Band positions are: I) 901-917 cm^{-1}, II) 975-1000 cm^{-1} (with the highest frequencies in peraluminous rhyolites), III) 1047-1060 cm^{-1}, IV) 1113-1126 cm^{-1}, and V) 1174-1182 cm^{-1}. The good quality of the fit is indicated by the randomness of the residuals. Fitting six components instead of five reduces the quality of the fit.

587 Concerning CO_2-bearing basanitic glasses, best fitting in the 630-1200 cm^{-1} spectral
588 range was achieved with six to seven components, whose positions are: I) 707-715 cm^{-1}, II)
589 779-789 cm^{-1}, III) 864-891 cm^{-1}, IV) 930-963 cm^{-1}, V) 990-1021 cm^{-1}, VI) 1061-1077 cm^{-1}
590 and VII) 1084-1088 cm^{-1} (Fig. 3S, Table 2S). The last component refers to the ν_1 Raman
591 vibration of dissolved carbonate (Morizet et al., 2013).

592 Peak fitting of the total water band requires a minimum of four Gaussian components
593 (Table 3S, Fig. 4S), in agreement with previous studies (e.g., Chabiron et al., 2004; Behrens
594 et al., 2006; Di Muro et al., 2006). The positions of these components are: I) 3080-3098 cm^{-1},
595 II) 3250-3298 cm^{-1}, III) 3420-3487 cm^{-1} (with the highest frequencies in rhyolites), IV) 3540-
596 3575 cm^{-1}, and V) 3600-3645 cm^{-1} (with the lowest frequencies in basanites and basalts);
597 these positions match those determined by Di Muro et al. (2006). The small component I is
598 only present in water-rich glasses (Fig. 5), as observed by Behrens et al. (2006). In general,
599 the intensity of the low frequency components increases with total dissolved water, in
600 agreement with the expected increase of molecular water (e.g. Mysen and Virgo, 1986).

601 **5. DEPTH PROFILES**

602 Intensities (i.e. height of the dominant band) and integrated intensities (i.e. total area) of
603 the Raman bands vary with focusing depth of the laser beam (e.g., Behrens et al., 2006;
604 Mercier et al., 2009). Depth profiles measured in the alumino-silicate vibration region and
605 water region, under both high and standard confocality conditions, are shown in Fig. 7 for
606 basaltic, andesitic and rhyolitic compositions. Differences appear between glasses with
607 different compositions and absorptivities.

608 In the alumino-silicate domain of basanitic and basaltic glass spectra, signal intensity
609 increases from the surface to a depth of 2-3 µm and 3-4 µm in high and standard confocality,
610 respectively. The maximum intensity is 22% (basanitic) and 35 % (basalt) higher than the

signal intensity at the surface in high confocality, whereas it increases by ~45 % in standard confocality (Fig. 7). In andesitic glasses, maximum intensity, which is attained at 3-4 µm depth, is 50 % higher than the signal at the surface. Below the maximum normalized intensity, the intensity decreases with depth by 3 %/µm in the first 30 µm in basanitic glasses and by 2 %/µm in both basaltic and andesitic glasses (Fig. 7). Maximum alumino-silicate signal intensity in rhyolitic glasses is attained at ~5 µm depth in a highly confocal setting, but at 7-10 µm depth under standard confocality conditions. At these depths the intensity is 55 and 65 % higher (in high and standard confocality, respectively) compared to the one measured at the surface; then it diminishes by 1 %/µm (high confocality) and 0.5 %/µm (standard confocality) for the remainder of the first 30 µm.

Maximum signal intensity of the water band is attained at the same depths as for the alumino-silicate bands (Fig. 7). However, the percentages of increase with respect to signal at the surface are lower for water bands than observed for alumino-silicate bands. In the high confocality setting, the increase ranges from 15-18 % in basaltic and basanitic glasses to 20-25 % in andesitic and rhyolitic glasses, whereas in the standard confocality setting, it varies from 20-25 % in basaltic and andesitic glasses to 29-35 % in basanitic and rhyolitic glasses. That is, the intensity increase in the alumino-silicate region is twice as high as that in the water region. This causes the observed variability of the ratio between the intensity of the water band and the intensity of the silicate band ("OH/Si"). Below the depth of maximum signal intensity, Raman intensity of the water band decreases more slowly with depth compared to the alumino-silicate bands. Specifically, it drops by 2.6 %/µm in basanites, by 1.5 %/µm in basaltic and andesitic compositions, whereas it remains almost constant over 12 µm in rhyolitic glasses before dropping by 0.7 %/µm. The evolution with depth of the OH/Si band intensity ratio is significantly different in high and standard confocality settings. Indeed, under less confocal conditions this ratio remains almost constant at minimum values within

636 the first 5-20 µm, irrespective of glass composition. In contrast, the OH/Si band intensity ratio
637 is much more sensitive to depth when using the high confocality setting. Thus, under confocal
638 conditions depth precision is required to get reproducible OH/Si values.
639 Measurements of peak height and area provided consistent results. Moreover, similar
640 depth profiles were obtained at laser power conditions ranging from 1 to 16 mW. In contrast,
641 the signal intensities of both alumino-silicate and water bands drop faster with depth when the
642 laser power on the sample is about 75 mW. This is especially relevant for basaltic glasses, in
643 which maximum signal intensity occurs at the glass surface at these high laser-power
644 conditions. These observations are consistent with more intense self-absorption expected in
645 basaltic glasses compared to more silica-rich glasses (e.g., Behrens et al., 2006; Mercier et al.,
646 2009). Excitation of (iron-bearing) basaltic samples, in fact, results in attenuation of both the
647 exciting light and the Raman scattered light.
648 Depths where both signals of the alumino-silicate and water bands are the highest were
649 considered as optimal focusing depths. For measurements performed in high confocality
650 setting, the adopted focusing depths correspond to the depth of minimum OH/Si band
651 intensity ratio. As shown in the following sections, this is a critical step to ensure a good
652 calibration. We highlight that a focusing error of about 1 µm near the depth of maximum
653 signal intensity causes a relatively small error (< 3% relative) in measured band intensity.
654 Larger focusing errors, however, result in non-negligible drop of the measured intensity.

655 **6. CALIBRATION**

656 ***6.1 External calibration method***

657 In the external calibration method, water concentration in an unknown glass sample is
658 derived from the absolute (integrated) intensity of the band at ~3570 cm^{-1} compared to band

659 (integrated) intensities of reference glasses with known water contents defining a calibration
660 line (e.g., Behrens et al., 2006; Di Muro et al., 2006; Mercier et al., 2010).

661 When spectra are treated using the described procedure for focus depth selection and
662 baseline correction, both I_{OH} and A_{OH} show positive linear correlation with glass water
663 contents determined by FTIR spectroscopy or SIMS. Correlations based on peak height
664 measurements, however, are affected by a larger scatter than correlations based on peak area
665 (Fig. 5S), therefore, only calibrations based on area measurements are considered hereafter.
666 Such a difference is explained by the observation that varying amounts of water dissolved in
667 glasses with different compositions produce not only variations in peak height, but also in
668 total band width and distribution of spectral components (as summarized in the previous
669 section).

670 Figure 8 (a to c) shows calibration lines obtained in high or standard confocality setting
671 after subtracting a cubic or a linear baseline from raw data. In these plots, reference glasses
672 define a single composition-independent linear relationship between water band intensity and
673 water concentration. The calibration based on cubic background subtraction provides the best
674 fit in both high confocality:

675 $$C_{H2O}\ (\text{wt\%}) = 2.403\ (\pm\ 0.033) \cdot A_{OH} - 0.058\ (\pm\ 0.046) \quad (R^2 = 0.995), \qquad (1)$$

676 and standard confocality setting:

677 $$C_{H2O}\ (\text{wt\%}) = 2.057(\pm\ 0.025) \cdot A_{OH} + 0.072\ (\pm\ 0.039) \quad (R^2 = 0.996). \qquad (2)$$

678 The data are reproduced with a root-mean-square error of ~0.13 and ~0.11 wt% in high and
679 standard confocality, respectively (Fig. 8, Table 4S). The linear regressions do not take into
680 account the uncertainties on H_2O content of the reference glasses. Their intercepts pass very
681 close to the origin. Linear calibrations with similar slopes (within 15 % difference) were

682 reproduced using a range (1-16 mW) of laser powers in different sessions over several
683 months.

684 It is worth noting that measurements performed by focusing the laser beam on the
685 surface of the alumino-silicate glasses yielded slightly divergent calibration lines whose
686 slopes depend on glass composition: the slope decreases from basaltic to rhyolitic
687 compositions, as previously observed by Mercier et al. (2010).

688 ***6.2 Internal calibration method***

689 The internal calibration procedure is based on the correlation between the glass water
690 concentration and the relative (integrated) intensities of the water and alumino-silicate Raman
691 bands. To compare spectra of alumino-silicate glasses with different compositions, and
692 because Mercier et al. (2009) reported a significant effect of bulk chemical composition on
693 internal calibrations based on normalization to either LF or HF band heights, we built our
694 internal calibration procedure on the measurement of band total area, instead of band height
695 (Fig. 9).

696 OH/Si increases with water content and the increase is generally higher for mafic than
697 for felsic glasses (Fig. 9a). Between the two felsic compositions, the increase of the OH/Si
698 ratio with water of the peraluminous rhyolite is noticeably more important than the
699 peralkaline one. More precisely, calcalkaline and tholeiitic glasses bearing less than 3 wt %
700 H_2O and the peraluminous rhyolite with various water contents fit on a single trend, whereas
701 the other glasses diverge from the general trend to higher OH/Si ratios (the water-rich basalts)
702 or lower OH/Si ratios (the basanites and peralkaline rhyolites) (Fig. 9a). Similar trends are
703 obtained when subtracting a linear/cubic baseline from raw or Long-corrected data.
704 Measurements performed in a standard confocality setting (not shown) yield a ~50 % steeper
705 calibration line than measurements done under high confocality conditions.

706 The divergence of water-rich basalts and peralkaline rhyolites from the main trend in
707 Fig. 9a is due to the effect of water content on the integrated intensity of the alumino-silicate
708 region and to the behavior of the band at 980 cm^{-1}, respectively. Careful inspection of spectra
709 in the alumino-silicate vibration region reveals that the integrated intensity (hereafter $A_{Al\text{-}Si}$)
710 of this region generally decreases with increasing water content and decreasing density (Fig.
711 10), regardless of analytical conditions (i.e. laser power on sample and confocality) and
712 baseline treatment, except for the peralkaline and basanitic glasses. The effect of water in
713 lowering $A_{Al\text{-}Si}$ is maximum in basaltic glasses, in particular in the 82-72f set with 30 %
714 intensity reduction for 15 mol % H_2O (Fig. 10 c), and becomes smaller in andesitic and
715 rhyolitic glasses characterized by < 12 % and 10 % reduction for 18 mol % H_2O and 25
716 mol % H_2O, respectively (Fig. 10 e, g). In CO_2-bearing basanitic glasses, the observed
717 increase of $A_{Al\text{-}Si}$ with decreasing density (Fig. 10 b) is due to the presence of CO_3^{2-} dissolved
718 in these glasses; the intensity of the ν_1 Raman vibration of dissolved carbonate at ~1087 cm^{-1}
719 (Fig. 3S) has to be subtracted from the intensity of the alumino-silicate envelope (Table 2S).
720 Adjustments of the internal calibration method to take into account the effect of water content
721 on $A_{Al\text{-}Si}$, the behavior of the band at 980 cm^{-1} in peralkaline rhyolites and the presence of
722 CO_3^{2-} in basanites are presented in the Discussion section.
723 Small deviations from the general trends of Fig. 10 in a given set of glasses reflect
724 differences in glass structure. For instance, the higher $A_{Al\text{-}Si}$ measured in the A071215 sample
725 is probably due to a different iron oxidation state compared to the other andesitic glasses (see
726 spectra of Fig. 4c). The HF band in A310317 and A030417 glass spectra contains an
727 additional contribution from the vibration of CO_3^{2-} molecules (Fig. 10 e). The basaltic sample
728 82-72f#10 is characterized by a larger $A_{Al\text{-}Si}$ than expected from the general trend of the 82-
729 72f basaltic set (Fig. 10 c). This may be due to the slightly higher density of this sample
730 compared to the other glasses of the same basaltic set (Fig. 2). Analogously, the higher

731 synthesis pressure (and thus the relatively higher density) of the basanite BSN101117-2
732 compared to the other basanitic glasses (Table 1) may be partly responsible for its
733 significantly larger $A_{Al\text{-}Si}$ (Fig. 10 a, b).

734 **7. DISCUSSION**

735 ***7.1. Parameters controlling the Raman signal***

736 Raman vibration intensity of a molecule is proportional to the quantity of the analyzed
737 molecule and to its Raman scattering cross-section (which expresses the Raman scattering
738 efficiency of a molecule) (e.g. Dubessy et al., 2012), but it depends also on analytical
739 conditions and instrumental features that influence the excited volume (e.g., laser wavelength
740 and power, confocal aperture of slits or pinholes, microscope magnification, numerical
741 aperture of the objective, grating). These relationships are expressed in the following
742 equation:

743 $$N = N_{V0}/A \cdot d\sigma/d\Omega \cdot \Delta\Omega \cdot N_m \quad (3)$$

744 where N is the total number of Raman photons for a specific vibrational mode, N_m is the
745 number of molecules contained in the scattering volume V that are responsible for that
746 vibrational mode (i.e. $N_m = \rho V$ if ρ is the number of molecules per unit volume), $d\sigma/d\Omega$ is the
747 differential Raman scattering cross-section of a specific Raman mode, N_{V0}/A is the flux of
748 photons of the laser focused onto the sample area A, and $\Delta\Omega$ is the solid angle of light
749 collection.

750 Previous studies showed that the Raman scattering cross-section of different Q^n species
751 and dissolved hydrous species depends on glass composition and structure (Fukumi et al.,
752 1990; Zotov 2001; Zajacz et al., 2005; Behrens et al., 2006; Mercier et al., 2010). Mercier et
753 al. (2010) highlighted that the matrix effect on the total water band is related to differences in

754 glass reflectance and water bonding environment. Moreover, they reported positive
755 correlations between the slope of the calibration line and both reflectance and density of the
756 glass.

757 The size of the scattering volume of the glass is affected by its physico-chemical
758 characteristics such as chemical composition, structure, density, reflectance, refractivity and
759 absorptivity. The confocal scattering volume can be expressed by the product of the
760 illumination volume (i.e. the volume of the laser focus) and the detection volume (which is
761 defined by Raman photons generated within the illumination volume that are relayed back
762 into the spectrometer via the confocal aperture, Everall, 2004; Maruyama and Kanematsu,
763 2011). In particular, these two volume components determine the depth resolution of Raman
764 measurements. Therefore, in order to interpret correctly confocal Raman measurements, one
765 should take the spread in focal position due to light refraction into account (Everall, 2004;
766 Maruyama and Kanematsu, 2011). When focusing beneath the surface of a sample with a
767 refraction index above 1, the light rays are slowed down and refracted according to Snell's
768 law. In general, upon moving deeper into the sample the axial laser focus broadens and focus
769 position shifts to lower depth than indicated by microscope vertical displacement, because
770 depth resolution degrades with depth below the surface (Everall, 2004; Maruyama and
771 Kanematsu, 2011). These processes can explain the different depth profiles and distinct slopes
772 of the calibration lines we obtained when changing from high confocality to standard
773 confocality settings (Figs. 7 and 8). Because the observed shapes of OH/Si depth profiles vary
774 with confocality (Fig. 7), we expect these differences to be reflected in calibration lines.
775 Different slopes of the internal calibration lines obtained for high and standard confocality
776 conditions suggest that the internal calibration does not correct for the effect due to changes in
777 confocal volume size.

7.2. External versus internal calibration

Concerning the external calibration, the linear relationship between water contents (as determined by FTIR or SIMS) and A_{OH} (Fig. 8) can be explained in two ways: either the scattering cross-section of the water stretching vibration mode is independent of the glass matrix composition, or the procedure established for spectra acquisition and baseline treatment minimizes the differences in Raman cross-section and the effects related with size of the confocal volume, self-absorption and reflectance at the sample surface. Taking into account the findings of previous studies (e.g. Mercier et al., 2010), we believe this second hypothesis is more likely. Small differences in shape and componentry between the water bands of the studied glasses (Fig. 5 and Fig. 4S) are consistent with differences in water bonding environments and speciation, as previously discussed by Behrens et al. (2006), Di Muro et al. (2006b) and Mercier et al. (2010). The external calibration method proposed here yields a single calibration line allowing analysis of all alumino-silicate glasses with the same level of accuracy as previous studies (e.g., Behrens et al., 2006). This suggests that measurements performed following the procedure established in this study (i.e., measurements performed at optimal focus depths rather than on sample surface, and based on quantification of the water band area instead of band height) provide the best conditions for correction of differences in Raman scattering efficiency between glasses with variable subalkaline and alkaline compositions.

In the case of internal calibration, the intensity of the water band is scaled to the alumino-silicate band intensity, resulting in a stronger dependence on glass composition (Fig. 9a), in agreement with previous works (e.g., Zajacz et al. 2005, Mercier et al. 2009). To better compare all the glass sets, the CO_2-bearing glasses need to be corrected for the contribution of the CO_3^{2-}-related spectral component (Fig. 3S). This is simply achieved by multiplying the

802 $A_{Al\text{-}Si}$ by a factor that takes into account the contribution of the component VII relative to the
803 sum of the areas of all spectral components (Table 2S). In line with the results of Morizet et
804 al. (2013), we found that the relative contribution of the CO_3^{2-} is proportional to the total CO_2
805 content.

806 The observed relationships between $A_{Al\text{-}Si}$, glass density and water content (Fig. 10)
807 indicate that glass density strongly affects Raman scattering of the alumino-silicate vibration
808 region. When we consider the glass density dependence, by normalizing the intensity of the
809 alumino-silicate envelopes to the intensity measured in anhydrous glasses, the studied glasses
810 define a single positive linear correlation, except for the peralkaline ones (Fig. 9b). This linear
811 relationship is expressed by the following equation:

812 $$OH/Si = [A_{OH}/(p \cdot t_1)]/[A_{Al\text{-}Si}/(p \cdot t_2) \cdot (1 + \alpha_1)] \quad (4)$$

813 where $\alpha_1 = 1 - (A_{Al\text{-}Si\ hydrous}/A_{Al\text{-}Si\ anhydrous})$, p is the laser power, and t_1 and t_2 are the acquisition
814 times in the water and alumino-silicate regions, respectively. In other words, the correction
815 factor (α_1, Table 4S) is proportional to the difference between the $A_{Al\text{-}Si}$ of the anhydrous glass
816 and that of the hydrous glasses of each set (Fig. 10). The correction factor depends on both
817 glass composition and water content (see Fig. 2); either density or mol% H_2O estimated with
818 the external calibration method can be used to estimate α_1 (Fig. 10). Up to ~7 wt % H_2O
819 contents, rhyolitic, andesitic and basanitic glasses require a minor correction (< 10-12 % in
820 the studied range of water contents). In contrast, water-rich (> 3 wt % H_2O) basaltic glasses
821 need more important corrections.

822 Peralkaline glasses are well aligned below the calibration line defined by peraluminous
823 rhyolites (Fig. 9a). In order to understand their distinct behavior, we performed peak fitting of
824 the alumino-silicate HF envelope of both peralkaline and peraluminous glasses (Fig. 6). The
825 spectral components I, IV and V are more important in peraluminous rhyolites than in

peralkaline ones, whereas the opposite behavior is observed for the components II and III. The sum of the components III, IV and V represents approximately 50 % of the total area in both glass sets (51 ± 6, 1σ). In contrast, the sum of the areas of the components I, II and III varies significantly from peraluminous (~50 % of the total area) to peralkaline (70-75 % of the total area) glasses, with a 20-25 % difference. This difference can be explained by the higher Fe content and oxidation state of peralkaline glasses, as revealed by the sharp increase of the component (II) at ~980 cm^{-1}, which is attributed to the presence of four-fold coordinated Fe^{3+} in alkali-bonded Q^3 units (e.g., Wang et al., 1995; Di Muro et al., 2009; Di Genova et al., 2016). The internal calibration procedure can be improved by taking into account the high Raman scattering of the 980 cm^{-1} band in peralkaline rhyolites, and this can be performed by calculating a correction factor:

$$\alpha_2 = [100 - ((\text{I-II-III})_{\text{peralkaline}} - (\text{I-II-III})_{\text{peraluminous}})]/100 \quad (5)$$

where (I-II-III) represent the sum of the areas of the components I, II and III (Table 1S). Once the $A_{Al\text{-}Si}$ of peralkaline glasses is corrected for the difference in componentry compared to peraluminous glasses, all rhyolitic glasses follow the same calibration line defined by all other compositions (Fig. 9c). This observation suggests that Fe^{3+} has an important effect on the Raman scattering efficiency of alumino-silicate glasses; in rhyolitic glasses the vibrational mode at 970-980 cm^{-1} has an important Raman scattering cross-section.

The linear fit of the internal calibration is expressed by the following equation (Fig. 9c):

$$C_{H2O}\ (\text{wt\%}) = 2.179\ (\pm\ 0.037) \cdot A_{OH}/A_{Al\text{-}Si\ corr} + 0.060\ (\pm\ 0.055) \quad (R^2 = 0.992), \quad (6)$$

where $A_{Al\text{-}Si\ corr}$ is the corrected area of the alumino-silicate envelope and $A_{OH}/A_{Al\text{-}Si\ corr}$ (i.e., OH/Si in Fig. 9c) = $A_{OH}/(\alpha_1 \cdot A_{Al\text{-}Si} + \alpha_2 \cdot A_{Al\text{-}Si})$. The linear fit reproduces the whole dataset within 0.17 wt % (root-mean-square error).

7.3. Application to natural glass inclusions

As a final step, we examine if the calibration procedures described in the previous sections can be applied to the study of natural hydrous glasses. We tested them on natural olivine-hosted glass inclusions from Santorini volcano, Lanzarote Island and FAMOUS Zone (Mid Atlantic Ridge) (Table 3). For the geochemical characterization of Santorini inclusions, including their volatile contents and details on secondary ion mass spectrometry (SIMS) measurements, we refer the reader to Druitt et al. (2016). Inclusions from Lanzarote have been studied by Gómez-Ulla et al. (*submitted*) and analyzed using a CAMECA ims-4f ion probe at the NERC Ion Microprobe Facility at the University of Edinburgh. The reader is referred to Schiavi et al. (2016) for details on the inclusions from FAMOUS Zone and FTIR measurements.

The studied inclusions have variable composition spanning from basanitic to basaltic and andesitic, and contain different amounts of water ranging from 0.1 to 3.3 wt% (Table 3). They contain less than 0.13 wt% CO_2, except for two basanitic inclusions, TAO-ol1 and TGN-ol18 bearing, respectively, 0.43 ± 0.09 and 0.21 ± 0.09 wt% CO_2. As CO_2 contents < 0.2 wt% are not detected using Raman spectroscopy (Morizet et al., 2013), only the two basanitic inclusions were corrected for the presence of dissolved carbonate. The relatively large size of the analyzed glass inclusions and the very weak or absent scattering from the embedding olivine crystals allowed focusing the laser beam at depths where the intensity of the water signal was maximum (-2 or -3 μm). These correspond to the optimal depths reported in Figure 7 for the reference glasses.

We were unable to test our calibration procedure on silica-rich glasses with dacitic or rhyolitic compositions because all the tested inclusions contained magnetite nanocrystals, as revealed by the intense scattering of a Raman band near 670 cm^{-1} (Frezzotti et al., 2012). In line with the findings by Di Genova et al. (2017), we observed that presence of Fe-oxides

874 dispersed in the glass causes underestimation of the water content of the inclusion, most likely
875 due to light absorbance and possible heating and oxidation of the oxide phases.
876 Figure 8d shows the results of the external calibration procedure applied to glass
877 inclusions. The estimated water contents are in very good agreement with SIMS
878 measurements and provide information about the accuracy of the method. The average
879 relative standard deviations (RSD) between Raman and SIMS analyses are ~3 % and 5 % (1σ)
880 when using a cubic or a linear baseline correction, respectively. It is worth noting that SIMS
881 measurements were carried out first, so we cannot exclude that some water loss occurred from
882 the inclusion before Raman analyses. For glass inclusions bearing H_2O contents close to the
883 detection limit of the method (i.e. ~0.1 wt%), the RSD between FTIR and Raman
884 measurements increases (4-22 %, with maximum values for cubic background subtraction),
885 partly due to decreasing signal/noise intensity ratio.
886 When using the internal calibration approach without applying the corrections (for
887 density and componentry) defined above, a first approximate estimate of the water dissolved
888 in the glasses is obtained (inset in Fig. 9a). Basaltic and andesitic inclusions fall close to the
889 main trend defined by the reference glasses, although some scatter is observed in inclusions
890 bearing ~3 wt% H_2O. The basanitic inclusions, instead, are aligned with the basanitic
891 reference glasses below the main trend.
892 On quantifying water in glass inclusions, we are faced with the difficulty of measuring
893 density of natural glass inclusions. Ardia et al. (2014) studied the evolution of haplogranite
894 glass structure with pressure and water content, and observed that at a fixed water content and
895 glass composition, density is a function of quench pressure. Thus, Raman spectra of melt
896 inclusions trapped over a large pressure range are potentially influenced by the trapping
897 pressure as well. In principle, the relationship observed between density, water content and
898 $A_{Al\text{-}Si}$ will hold when a set of natural glass inclusions with similar composition that were

quenched from similar pressure are analyzed, regardless of the absolute value of their density and quench pressure. In this case, corrections can be attempted within each set of glass inclusions based on the relationship between water contents estimated using the external calibration method and $A_{Al\text{-}Si}$. In some cases, calculating the density of glass inclusions could help decreasing the uncertainties of the method. Where these methods cannot be applied, water quantification should be performed based on reference glasses with similar composition, which do not require density-related correction.

Attempts to estimate the density-related factor α_1 for the studied inclusions resulted in non-negligible uncertainties on the OH/Si ratio. This is mainly due to the small number of analyzed inclusions with similar composition that did not allow defining trends as in Fig. 10 without uncertainty. For a qualitative analysis, the compositions of the inclusions, not corrected for density, are plotted on the main density-corrected trend defined by the reference glasses (inset in Fig. 9c). The observed distribution of the glass inclusions is in line with our expectations based on the behavior of the reference compositions (Fig. 10): the andesitic glass falls on the main trend as it is not expected to be strongly influenced by the density correction, several basaltic inclusions fall slightly above the main trend as observed for non-corrected reference basalts, while basanitic inclusions behave analogously to the reference basanites. Although this may be speculative, the strong similarities observed between reference samples and uncorrected glass inclusions probably suggest that differences of quench pressure in the studied inclusions has a minor influence on the established water quantification procedures.

CONCLUDING REMARKS

This study contributes to the ongoing research dedicated to the development of precise micro-Raman routines for water quantification in alumino-silicate hydrous glasses. Here we summarize the main new findings of our study.

We examined in detail how the Raman intensities of the water band and the alumino-silicate envelope change with confocality performance and focus depth of the laser beam, as previously investigated (e.g., Behrens et al., 2006; Mercier et al., 2009). We found that the extent of increase of water band intensity with focus depth is lower than that measured in the alumino-silicate envelope. This results in a variable OH/Si band intensity ratio, and highlights the importance of measuring glasses at their optimal focus depth, which corresponds to the depth of maximum intensity of the water band and minimum OH/Si ratio. The optimal focus depth depends on glass composition and confocal performance of the Raman instrument, and is expected to change with laser wavelength as well. Maximum intensity in both water and alumino-silicate regions is attained at 2-3 µm, 3-4 µm and 5-10 µm depth, respectively in basanitic-basaltic, andesitic and rhyolitic glasses under the instrumental and analytical conditions used in this study.

Thirty reference glasses belonging to both alkaline and subalkaline magmatic series and bearing up to ~7 wt % H_2O define a single external calibration line when they are analyzed at their optimal focus depth. In contrast, measurements performed on the sample surface did not yield a single calibration curve for glasses of different compositions. Our study suggests that water content of unknown samples can be determined based on a minimum of two reference glasses whose compositions do not need to match that of the unknown samples. However, using three or more reference glasses is recommended to improve the accuracy of water content quantification. In general, accurate water quantification using the external calibration

method requires careful, repeated measurement of reference glasses because small variations in laser power can occur during long analytical runs, lowering the analytical precision.

For the reasons illustrated above, depth profile measurements are important even when using the internal calibration method for water quantification, because the normalization to the intensity of the alumino-silicate envelope does not cancel completely the differences in confocal volume size, as previously expected. A universal calibration curve for quantification of water content in glasses cannot be established, unless the dependence of the confocal volume on different instrumental parameters is accurately known. Sharing common reference glasses between different laboratories may help future work for establishing a universal calibration.

This study recognizes critical parameters related with glass density, presence of ferric iron and dissolved carbonates as mainly responsible for matrix effects on the internal calibration method. We provide simple procedures for correcting and/or minimizing the effects of these parameters. Increasing water content lowers glass density and results in reduction of the area of the alumino-silicate envelope ($A_{Al\text{-}Si}$); we measured up to 30% intensity reduction in a high-Al basaltic glass bearing 15 mol% water. The correction method that we propose is based on the relative difference between $A_{Al\text{-}Si}$ of anhydrous and hydrous glasses with similar composition.

Peak fitting of the alumino-silicate high frequency envelope (approximately located between 800 and 1250 cm^{-1}) is required to quantify the intense scatterings around 980 cm^{-1} and 1080 cm^{-1} caused, respectively, by Fe^{3+} in four-fold coordination and CO_3^{2-} dissolved in glasses. Concerning the Fe^{3+}-related matrix effect, we must point out that, in principle, all Fe^{3+}-bearing glasses should be corrected for it. Nevertheless, only peralkaline rhyolites were corrected in this study because the area of the high frequency envelope in peralkaline

rhyolites is far more sensitive to changes in Fe^{3+}/Fe_{tot} than in mafic compositions (Di Muro et al., 2009; Di Genova et al., 2016). Once the proposed corrections are performed, all the studied glasses define a single internal calibration line in spite of their compositional variability. Alkaline glasses, specifically basanites, behave coherently with the other glass compositions when the analytical strategies and data treatment procedures (i.e., for baseline subtraction, peak fitting and density correction) established in the present study are used.

Accuracy of the external calibration in the high confocality setting was determined by testing our method on olivine-hosted glass inclusions whose water content was measured using SIMS or FTIR. The calculated average RSD is ~4% (1σ) for most samples, and increases to ~12% (1σ) for glass inclusions with H_2O contents close to the detection limits (~0.1 wt%).

Because of their specific textural complexities, natural glass inclusions provide a unique laboratory for testing further the proposed calibration method.

ACKNOWLEDGEMENTS

We acknowledge Claire Fonquernie for CHNS analyses. Nicolas Cluzel, Jean-Luc Devidal, Franck Pointud, Mhammed Benbakkar, and Geeth Manthilake are warmly thanked for laboratory assistance. FS is grateful to Sébastien Maussang (Renishaw) for helpful discussion and to the scientific coordinator of ClerVolc, Tim Druitt, for supporting the Raman project. We thank Andrea Di Muro and an anonymous reviewer for their constructive comments. ACW acknowledges support from the NSERC discovery program and an Invited professor position from the Université Clermont-Auvergne of Clermont-Ferrand. SIMS analysis on basanitic glass inclusions at Cambridge was supported by NERC grant number IMF535/1114 to Dr. M. Edmonds. This research was financed by the French

990 Government Laboratory of Excellence initiative (ClerVolc LabEx), the Région Auvergne and
991 the European Regional Development Fund. This is ClerVolc contribution number 264.

992 **REFERENCES**

993 Andersen T. and Neumann E-R. (2001) Fluid inclusions in mantle xenoliths, *Lithos* **55**,
994 301-320.

995 Ardia P., Di Muro A., Giordano D., Massare D., Sanchez-Valle C. and Schmidt M.W.
996 (2014) Densification mechanisms of haplogranite glasse sas a function of water content and
997 pressure based on density and Raman data, *Geochim Cosmoch Acta* **138**, 158-180.

998 Behrens H. and Jantos N. (2001) The effect of anhydrous composition on water solubility
999 in granitic melts, *Am Min* **86**, 14-20.

1000 Behrens H., Roux J., Neuville D.R. and Siemann M. (2006) Quantification of dissolved
1001 H_2O in silicate glasses using confocal microRaman spectroscopy, *Chem Geol* **229**(1), 96-112.

1002 Brawer S.A. and White W.B. (1977) Raman spectroscopic investigation of the structure of
1003 silicate glasses (II). Soda-alkaline earth-alumina ternary and quaternary glasses, *J Non-Cryst*
1004 *Solids* **23**, 261-278.

1005 Carroll M.R. and Holloway J.R. (1994) Volatiles in Magmas, Reviews in Mineralogy, vol.
1006 30, Mineralogical Society of America.

1007 Cashman K.V. (2004) Volatile Controls on Magma Ascent and Eruption, in The State of
1008 the Planet: Frontiers and Challenges in Geophysics (eds R.S.J. Sparks and C.J.
1009 Hawkesworth), American Geophysical Union, Washington, D. C.

1010 Chabiron A., Pironon J. and Massare D. (2004) Characterization of water in synthetic
1011 rhyolitic glasses and natural melt inclusions by Raman spectroscopy, *Contrib Mineral Petrol*
1012 **146**, 485-492.

1013 Cluzel N., Laporte D., Provost A. and Kannewischer I. (2008) Kinetics of heterogeneous
1014 nucleation in rhyolitic melts: implications for the number density of bubbles in volcanic
1015 conduits and for pumice textures, *Contrib Mineral Petrol* **156**(6), 745–763.
1016 Di Genova D., Hess K-U., Chevrel M.O. and Dingwell D. (2016) Models for the
1017 estimation of Fe^{3+}/Fetot ratio in terrestrial and extraterrestrial alkali- and iron-rich silicate
1018 glasses using Raman spectroscopy, *Am Min* **101**, 943-952.
1019 Di Genova D., Sicola S., Romano C., Vona A., Fanara S. and Spina L. (2017) Effect of
1020 iron and nanolites on Raman spectra of volcanic glasses: a reassessment of existing strategies
1021 to estimate the water content, *Chem Geol* **475**, 76-86.
1022 Di Muro A., Giordano D., Villemant B., Montagnac G., Scaillet B. and Romano C. (2006a)
1023 Influence of composition and thermal history of volcanic glasses on water content as
1024 determined by micro-Raman spectrometry, *Appl Geochem* **21**, 802-812.
1025 Di Muro A., Villemant B., Montagnac G., Scaillet B. and Reynard B (2006b)
1026 Quantification of water content and speciation in natural silicic glasses (phonolite, dacite,
1027 rhyolite) by confocal microRaman spectrometry, *Geochim Cosmochim Acta* **70**, 2868-2884.
1028 Di Muro A., Métrich N., Mercier M., Giordano D., Massare D. and Montagnac G. (2009)
1029 Micro-Raman determination of iron redox state in dry natural glasses: application to
1030 peralkaline rhyolites and basalts, *Chem Geol* **259**, 78-88.
1031 Dixon E.J., Stolper E.M. and Holloway J.R. (1995) An experimental study of water and
1032 carbon dioxide solubilities in mid-ocean ridge basaltic liquids: Part I. Calibration and
1033 solubility models, *J Petrol* **36**, 1607–1631.
1034 Druitt T.H., Brenchley P.J., Gökten Y.E. and Francaviglia V. (1995) Late Quaternary
1035 rhyolitic eruptions from Acigöl Complex, central Turkey, *J Geol Soc Lon* **152**, 655-667.

1036 Druitt T.H., Mercier M., Florentin L., Deloule E., Cluzel N., Flaherty T., Médard E. and
1037 Cadoux A. (2016) Magma storage and extraction associated with plinian and interplinian
1038 activity at Santorini Caldera (Greece), *J Petrol* **57**, 461-494.
1039 Duan X. (2014) A general model for predicting the solubility behaviour of H_2O–CO_2 fluids
1040 in silicate melts over a wide range of pressure, temperature and compositions, *Geochim*
1041 *Cosmochim Acta* **125**, 582–609.
1042 Dubessy J., Caumon M-C., Rull F. and Sharma S. (2012) Instrumentation in Raman
1043 spectroscopy: elementary theory and practice. In: Dubessy J., Caumon M-C. and Rull F. eds.,
1044 Raman spectroscopy applied to Earth sciences and cultural heritage, EMU Notes in
1045 Mineralogy Vol. 12, European Mineralogical Union, London pp. 83-172.
1046 Everall N. (2004) Depth profiling with confocal Raman microscopy, part 1, *Spectroscopy*
1047 **19**(10), 22-27.
1048 Franz J.D. and Mysen B.O. (1995) Raman spectra and structure of BaO-SiO_2, SrO-SiO_2,
1049 and CaO-SiO_2 melts to 1600°C, *Chem Geol* **121**, 155-176.
1050 Freitas D., Manthilake G., Schiavi F., Chantel J., Bolfan-Casanova N., Bouhifd M.A. and
1051 Andrault D. (2017) Experimental evidence supporting a global melt layer at the base of the
1052 Earth's upper mantle, *Nat Commun* **8**, doi:10.1038/s41467-017-02275-9.
1053 Frezzotti M.L., Tecce F. and Casagli A. (2012) Raman spectroscopy for fluid inclusion
1054 analysis, *J Geochem Explor* **112**, 1-20.
1055 Fukumi K., Hayakawa J. and Komiyama T. (1990) Intensity of Raman band in silicate
1056 glasses, *J Non-Cryst Solids* **119**, 297-302.
1057 Furukawa T., Fox K.E. and White W.B. (1981) Raman spectroscopic investigation of the
1058 structure of silicate glasses. III. Raman intensities and structural units in sodium silicate
1059 glasses, *J Chem Phys* **75**, 3226.

Grove T.L., Parman S.W., Bowring S.A., Price R.C. and Baker M.B. (2002) The role of an H_2O-rich fluid component in the generation of primitive basaltic andesites and andesites from the Mt. Shasta region, N California, *Contrib Mineral Petrol* **142**, 375-396.

Haddadi B. (2016) Ascension et dégazage des magmas basaltiques: application aux volcans d'Islande et de la Chaîne des Puys. Ph.D. thesis, Univ. B. Pascal, Clermont-Ferrand, France.

Herzog F. and Zakaznova-Herzog V.P. (2011) Quantitative Raman spectroscopy: challenges, shortfalls, and solutions – Application to calcium silicate glasses, *Am Min* **96**, 914-927.

Iacovino K., Oppenheimer C., Scaillet B. and Kyle P. (2016) Storage and evolution of mafic and intermediate alkaline magmas beneath Ross Island, Antarctica, *J Petrol* **57**, 93-118.

King P.L., Vennemann T.W., Holloway J.R., Hervig R.L., Lowenstern J.B. and Forneris J.F. (2002) Analytical techniques for volatiles: A case study using intermediate (andesitic) glasses, *Am Min* **87**, 1077-1089.

Le Losq C., Neuville D., Moretti R. and Roux J. (2012) Determination of water content in silicate glasses using Raman spectrometry: implications for the study of explosive volcanism, *Am Min* **97**, 779-790.

Long D.A. (1977) Raman spectroscopy, 276 pp., MacGraw-Hill, New York.

Malfait W.J., Sanchez-Valle C., Ardia P., Médard E. and Lerch P. (2011) Compositional dependent compressibility of dissolved water in silicate glasses, *Am Min* **96**, 1402-1409.

Mandeville C.W., Webster J.D., Rutherford M.J., Taylor B.E., Timbal A. and Faure K. (2002) Determination of molar absorptivities for infrared absorption bands of H_2O in andesitic glasses, *Am Min* **87**(7), 813-821.

Maruyama Y. and Kanematsu W. (2011) Confocal volume in laser Raman spectroscopy depth profiling, *J Appl Phys* **110**, 103107.

Matson D.W., Sharma S.K. and Philpotts J.A. (1983) The structure of high-silicate glasses. A Raman spectroscopic investigation, *J Non-Cryst Solids* **58**, 323-352.

McMillan P. (1984) Structural studies of silicate glasses and melts – applications and limitations of Raman spectroscopy, *Am Min* **69**, 622-644.

McMillan P.F. and Remmele R.L. (1986) Hydroxyl sites in SiO_2 glass: a note on infrared and Raman spectra, *Am Min* **71**, 772-778.

McMillan P.F., Wolf G.H. and Poe B.T. (1992) Vibrational spectroscopy of silicate liquids and glasses, *Chem Geol* **96**, 351-366.

Médard E. and Groove T.L. (2008) The effect of H_2O on the olivine liquidus of basaltic melts: experiments and thermodynamic models, *Contrib Mineral Petrol* **155**, 417-432.

Mercier M., Di Muro A., Giordano D., Métrich N., Lesne P., Pichavant M., Scaillet B., Clocchiatti R. and Montagnac G. (2009) Influence of glass polymerisation and oxidation on micro-Raman water analysis in alumino-silicate glasses, *Geochim Cosmochim Acta* **73**, 197-217.

Mercier M., Di Muro A., Métrich N., Giordano D., Belhadj O. and Mandeville C.W. (2010) Spectroscopic analysis (FTIR, Raman) of water in mafic and intermediate glasses and glass inclusions, *Geochim Cosmochim Acta* **74**(19), 5641-5656.

Métrich N. and Wallace P. (2008) Volatile abundances in basaltic magmas and their degassing paths tracked by melt inclusions, in Minerals, Inclusions & Volcanic Processes, (eds K. Putirka & F. Tepley), *Rev Mineral Geochem* **69**, 363-402.

Morizet Y., Brooker R.A., Iacono-Marziano G. and Kjarsgaard B.A. (2013) Quantification of dissolved CO_2 in silicate glasses using micro-Raman spectroscopy, *Am Min* **98**, 1788-1802.

Mourtada-Bonnefoi C.C. and Laporte D. (2002) Homogeneous bubble nucleation in rhyolitic magmas: an experimental study of the effect of H_2O and CO_2, *J Geophys Res* **107**, doi:10.1029/2001JB000290.

Mysen B.O. and Virgo D. (1986) Volatiles in silicate melts at high pressure and temperature: 1. Interaction between OH groups and Si^{4+}, Al^{3+}, Ca^{2+}, Na^{+} and H^{+}, *Chem Geol* **57**, 303-331.

Mysen B.O., Virgo D., Harrison W.J. and Scarfe C.M. (1980) Solubility mechanisms of H2O in silicate melts at high pressures and temperatures: a Raman spectroscopic study, *Am Min* **65**, 900-914.

Neuville D.R., Cormier L. and Massiot D. (2004) Al environment in tectosilicate and peraluminous glasses: a ^{27}Al MQ-MAS NMR, Raman, and XANES investigation, *Geochim Cosmochim Acta* **68**, 5071-5079.

Ohlhorst S., Behrens H. and Holtz F. (2001) Compositional dependence of molar absorptivities of near-infrared OH-and H_2O bands in rhyolitic to basaltic glasses, *Chem Geol* **174**(1), 5-20.

Rossano S. and Mysen B. (2012) Raman spectroscopy of silicate glasses and melts in geological systems. In: Dubessy J., Caumon M-C. and Rull F. eds., Raman spectroscopy applied to Earth sciences and cultural heritage, EMU Notes in Mineralogy Vol. 12, European Mineralogical Union, London pp. 319-364.

Sanchez-Valle C., Gaillard F., Ghosh S. and Metzger K. (2015) Fluids and melts in planetary interiors: From crust to core-mantle boundaries, *Chem Geol* **418**, 1-5.

Schiavi F., Provost A., Schiano P. and Cluzel N. (2016) *P-V-T-X* evolution of olivine-hosted melt inclusions during high-temperature homogenization treatment, *Geochim Cosmochim Acta* **172**, 1-21.

Seifert F.A., Mysen B.O. and Virgo D. (1981) Structural similarity of glasses and melts relevant to petrological processes, *Geochim Cosmochim Acta* **45** (10), 1879-1884.

Severs M.J., Azbej T., Thomas J.B., Mandeville C.W. and Bodnar R.J. (2007) Experimental determination of H_2O loss from melt inclusions during laboratory heating: evidence from Raman spectroscopy, *Chem Geol* **237**, 358-371.

Sharma S.K., Mammone J.F. and Nicol M.F. (1981) Raman investigation of ring configurations in vitreous silica, *Nature* **292**, 140-141.

Shishkina T., Botcharnikov R.E., Holtz F., Almeev R.R., Jazwa A.M. and Jakubiak A.A. (2014) Compositional and pressure effects on the solubility of H_2O and CO_2 in mafic melts, *Chem Geol* **388**, 112-129.

Sigmarsson O. and Halldorsson S.A. (2015) Delimiting Bárðarbunga and Askja volcanic systems with Sr- and Nd-isotope ratios, *Jökull* **65**, 17-28.

Stolen R.H. and Walrafen G.E. (1976) Water and its relation to broken bond defects in fused silica, *J Chem Phys* **64**, 2623-2631.

Stolper E. (1982) Water in silicate glasses: an infrared spectroscopic study, *Contrib Mineral Petrol* **81**, 1-17.

Thomas R. (2000) Determination of water contents of granite melt inclusions by confocal laser Raman microprobe spectroscopy, *Am Min* **85**, 868-872.

Thomas R., Kamenetsky V.S. and Davidson P. (2006) Laser Raman spectroscopic measurements of water in unexposed glass inclusions, *Am Min* **91**, 467-470.

Wang Z., Cooney T.F. and Sharma S.K. (1995) In situ structural investigation of iron-containing silicate liquids and glasses, *Geochim Cosmochim Acta* **59**, 1571-1577.

Withers A.C. and Behrens H. (1999) Temperature-induced changes in the NIR spectra of hydrous albitic and rhyolitic glasses between 300 and 100 K, *Phys Chem Miner* **27**(2), 119-132.

Woelffel W., Claireaux C., Toplis M.J., Burov E., Barthel E., Shukla A., Biscaras J., Chopinet M-H. and Gouillart E. (2015) Analysis of soda-lime glasses using non-negative matrix factor deconvolution of Raman spectra, *J Non-Cryst Solids* **428**, 121-131.

Xue X. and Kanzaki M. (2004) Dissolution mechanisms of water in depolymerized silicate melts: constraints from ^{1}H and ^{29}Si NMR spectroscopy and ab initio calculations, *Geochim Cosmochim Acta* **68**, 5027-5057.

Zajacz Z., Halter W., Malfait W.J., Bachmann O., Bodnar R.J., Hirschmann M.M., Mandeville C.W., Morizet Y., Müntener O., Ulmer P. and Webster J.D. (2005) A composition-independent quantitative determination of the water content in silicate glasses and silicate melt inclusions by confocal Raman spectroscopy, *Contrib Mineral Petrol* **150**, 631–642.

Zotov N. (2001) Effects of composition on the vibrational properties of sodium silicate glasses, *J Non-Cryst Solids* **287**, 231-236.

Zotov N. and Keppler H. (1998) The influence of water on the structure of hydrous sodium tetrasilicate glasses, *Am Min* **83**, 823-834.

Zotov N., Yanev Y., Epelbaum M. and Konstantinov L. (1992) Effect of water on the structure of rhyolite glasses – X-ray diffraction and Raman spectroscopy studies, *J Non-Cryst Solids* **142**, 234-246.

FIGURES

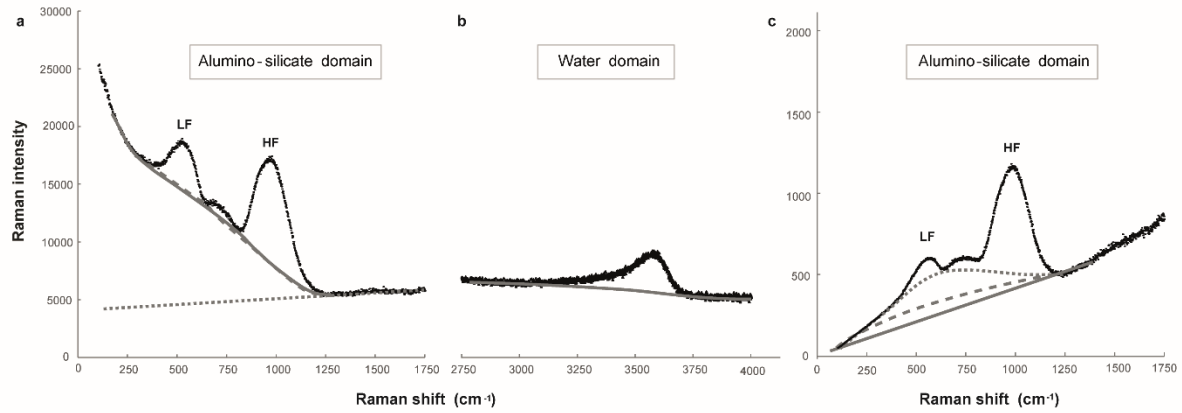

Fig. 1. Procedures for background subtraction used in previous studies. (a-b) Baseline fitting on raw Raman spectra. (a) In the alumino-silicate domain: cubic baseline (Mercier et al., 2009; dashed curve), cubic spline baseline (Behrens et al., 2006; continuous curve), and linear extrapolation method by Zajacz et al. (2005, dotted line); (b) cubic baseline in the water domain. (c) Baseline fitting on Long-corrected spectra in the alumino-silicate domain: cubic baseline (Di Muro et al., 2009; dashed curve) and cubic spline baseline (Behrens et al., 2006; continuous line) anchored at the extremities of the domain, or to a limited number of intermediate minima (Le Losq et al., 2012; dotted curve). LF and HF indicate low-frequency and high-frequency bands.

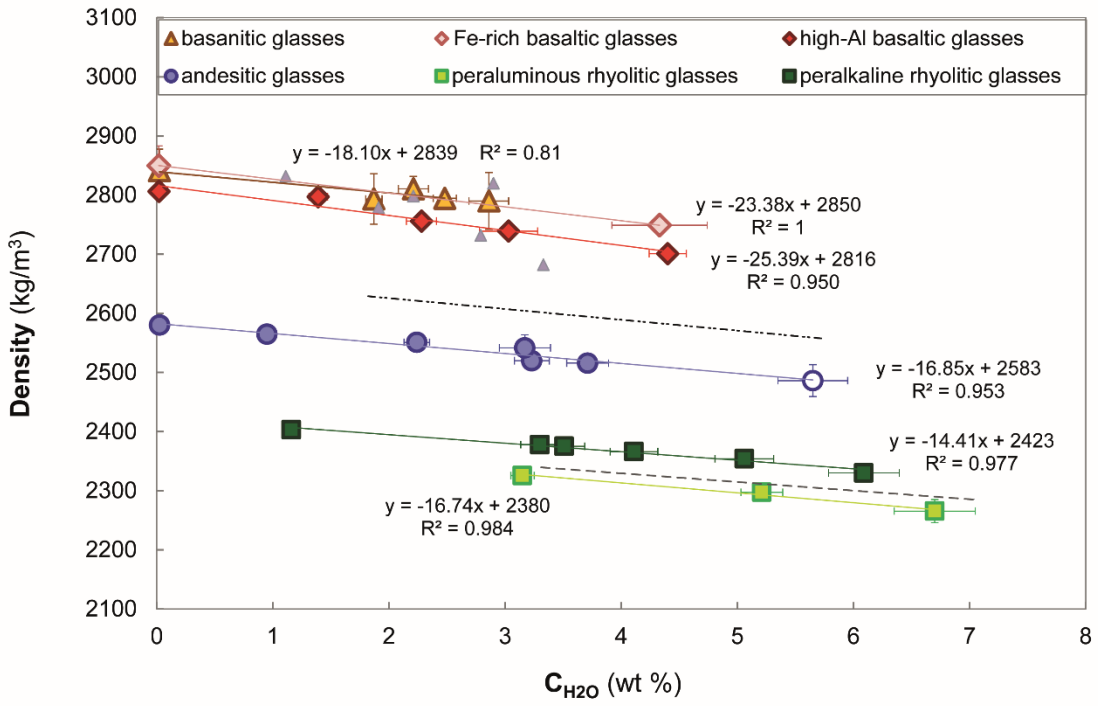

1189

1190 **Fig. 2.** Glass density versus glass water content determined by FTIR or SIMS
1191 measurements (see Table 1). A decrease of slope value from basaltic to rhyolitic glasses is
1192 observed. The dashed line represents the density of rhyolitic glasses calculated from Behrens
1193 et al. (2006). The dashed-dotted line shows the density of andesitic glasses determined by
1194 Ohlhorst et al. (2001). Small grey triangles are calculated basanitic glass densities by Iacovino
1195 et al. (2016). Microlite-bearing A011215 glass is the andesitic glass with the highest water
1196 content (empty circle). WM23-3 and 82-72f#19 glasses are not plotted because their densities
1197 were calculated, not measured.

1198

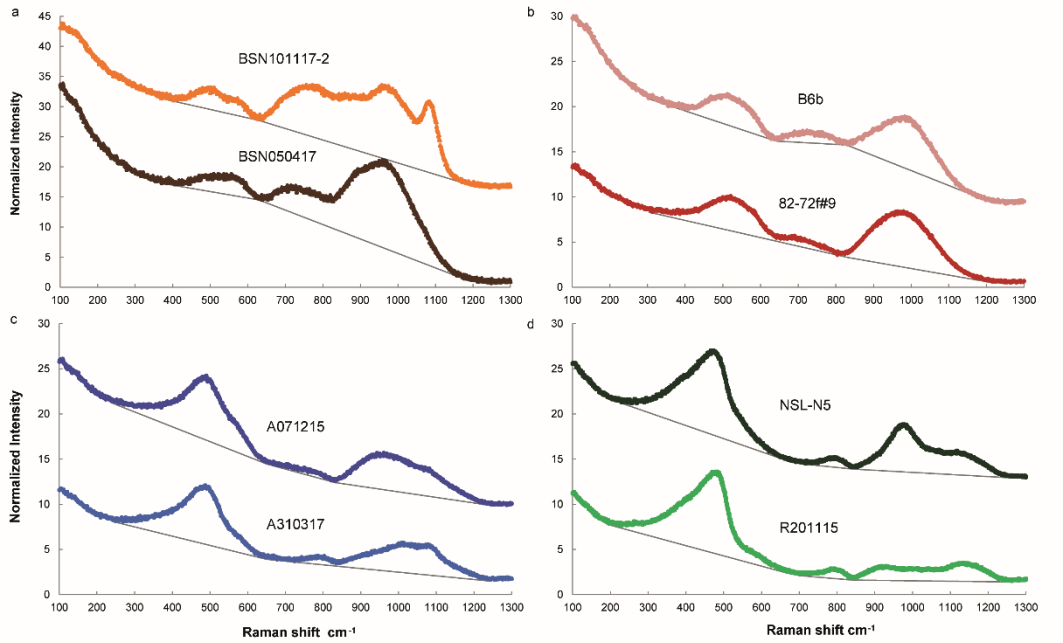

1199

1200 **Fig. 3**. Raw Raman spectra of the alumino-silicate vibration bands of the glasses with
1201 basanitic (a), basaltic (b), andesitic (c) and rhyolitic (d) compositions. Linear baselines
1202 adopted for background subtraction are shown with anchor points. Spectra are displaced
1203 vertically for clarity. Intensities were normalized to laser power and acquisition time.

1204

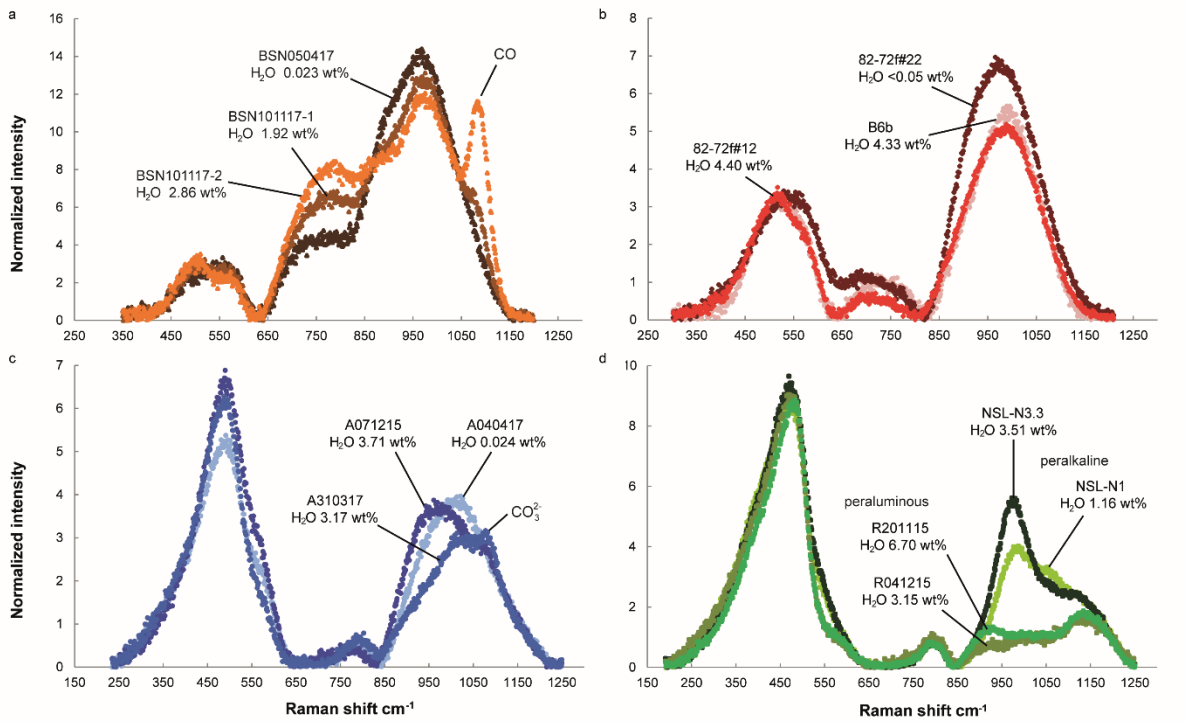

1205

1206 **Fig. 4**. Alumino-silicate region of raw Raman spectra of basanitic (a), basaltic (b),
1207 andesitic (c) and rhyolitic (d) glasses after subtraction of linear baselines. Spectra were
1208 measured under the same conditions of laser power and confocality. Intensities were
1209 normalized to acquisition time. Laser beam was focused at the optimal depth as defined in the
1210 text. Note differences in band topology associated with different major element compositions,
1211 water contents, degree of polymerization, and oxidation state (see text).

1212

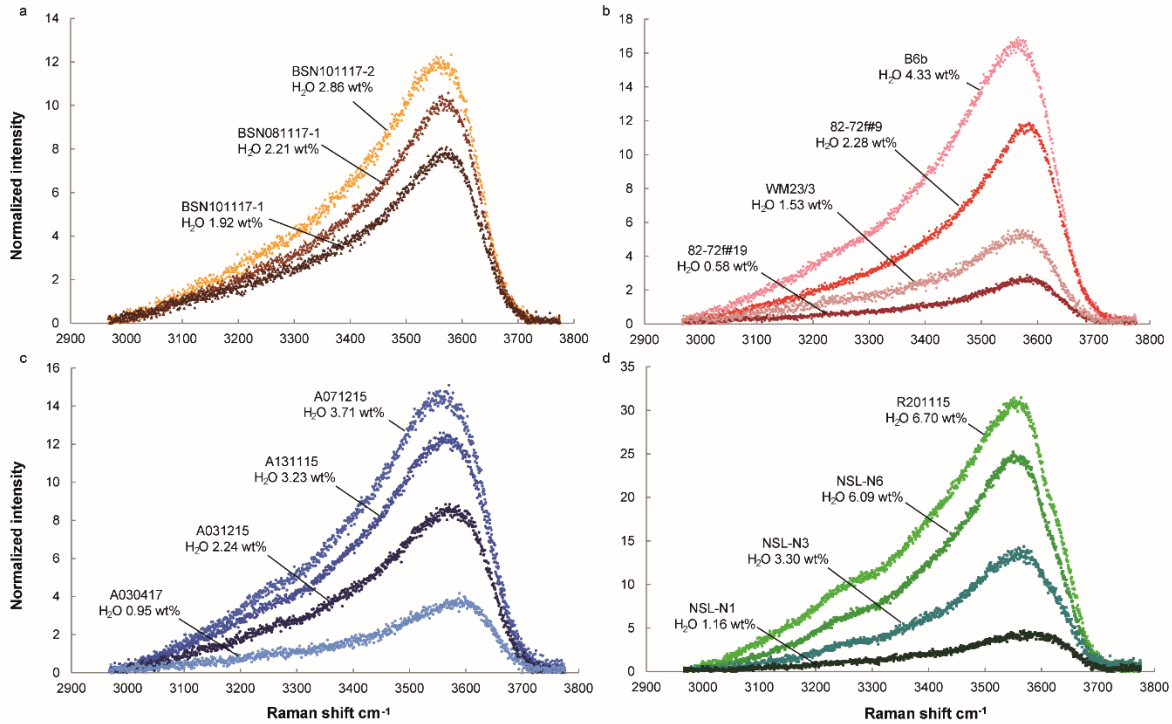

1213

1214 **Fig. 5**. Baseline-corrected Raman spectra in the water region of reference glasses:
1215 basanites (a), basalts (b), andesites (c) and rhyolites (d) with different water contents. Spectra
1216 were measured under the same conditions of laser power and confocality. Intensities were
1217 normalized to acquisition time. Laser beam was focused at optimal depths as defined in the
1218 text.

1219

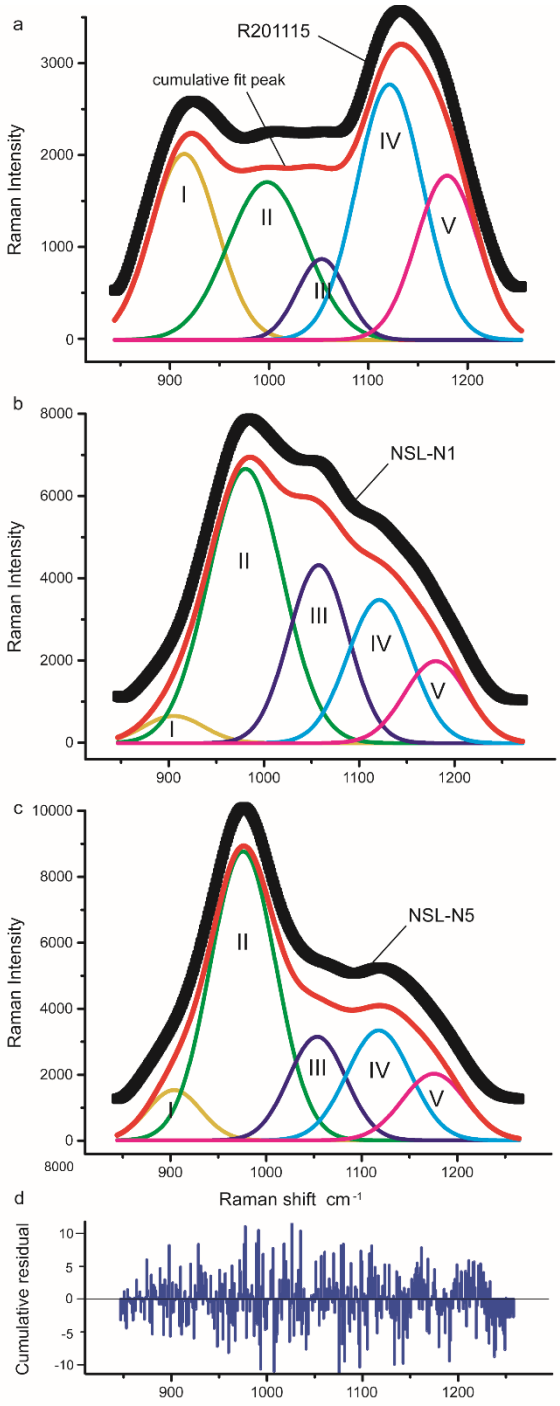

1220

1221 **Fig. 6.** Peak fitting of the HF alumino-silicate envelope of peraluminous (a), water-poor
1222 (b) and water-rich peralkaline (c) rhyolitic glasses with a finite number of Gaussian
1223 components performed with OriginPro software. The good quality of the fit is indicated by
1224 the randomness of the residuals (d).

1225

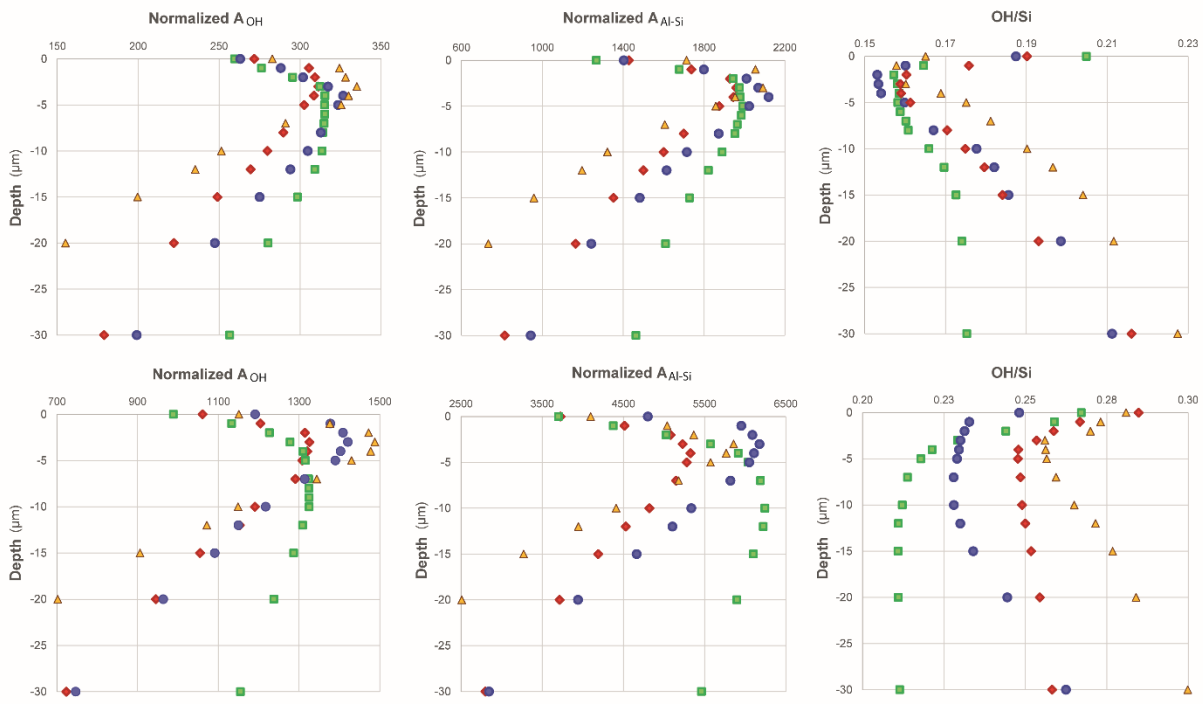

Fig. 7. Depth profiles measured in the water and alumino-silicate vibration regions of basanitic (yellow triangles), basaltic (red diamonds), andesitic (blue circles) and rhyolitic (green squares) glasses under high (upper row) and standard (lower row) confocality conditions. Integrated intensities of the water band (A_{OH}) and the alumino-silicate envelope ($A_{Al\text{-}Si}$) were normalized to laser power and acquisition time; water band intensities were also normalized to water content.

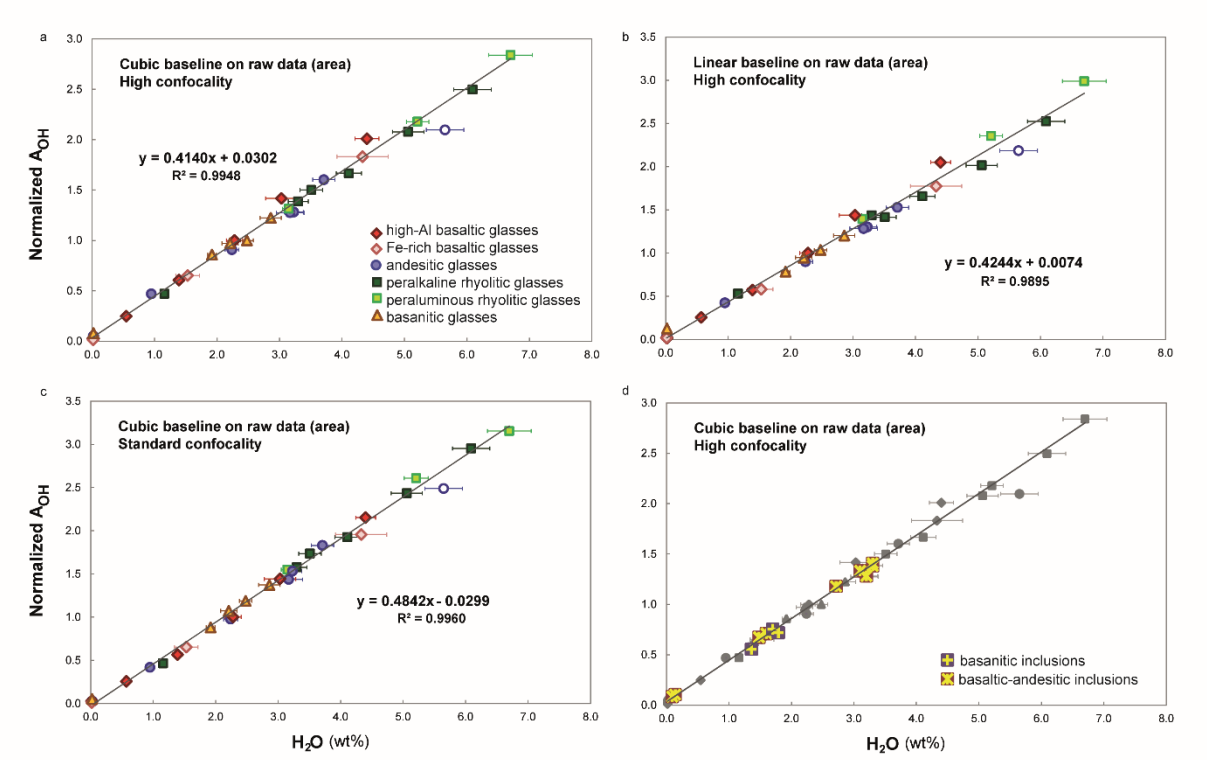

1234

1235 **Fig. 8.** External calibration lines for quantification of water contents in glasses, obtained
1236 after subtracting a cubic or a linear baseline from raw data: areas in high confocality setting
1237 (a-b, d), and in standard confocality setting (c). Reference glasses define a composition-
1238 independent linear relationship. In (d) glass inclusions are plotted over the reference glasses.
1239 Microlite-bearing A011215 glass (empty circle) is shown but is not considered for calibration
1240 line definition. Water band areas were normalized to the water band area of the 82-72f#9
1241 basaltic glass, which was used as internal standard to eliminate small variations in
1242 measurement conditions. For glass inclusions, errors associated with SIMS measurements are
1243 smaller than symbols.

1244

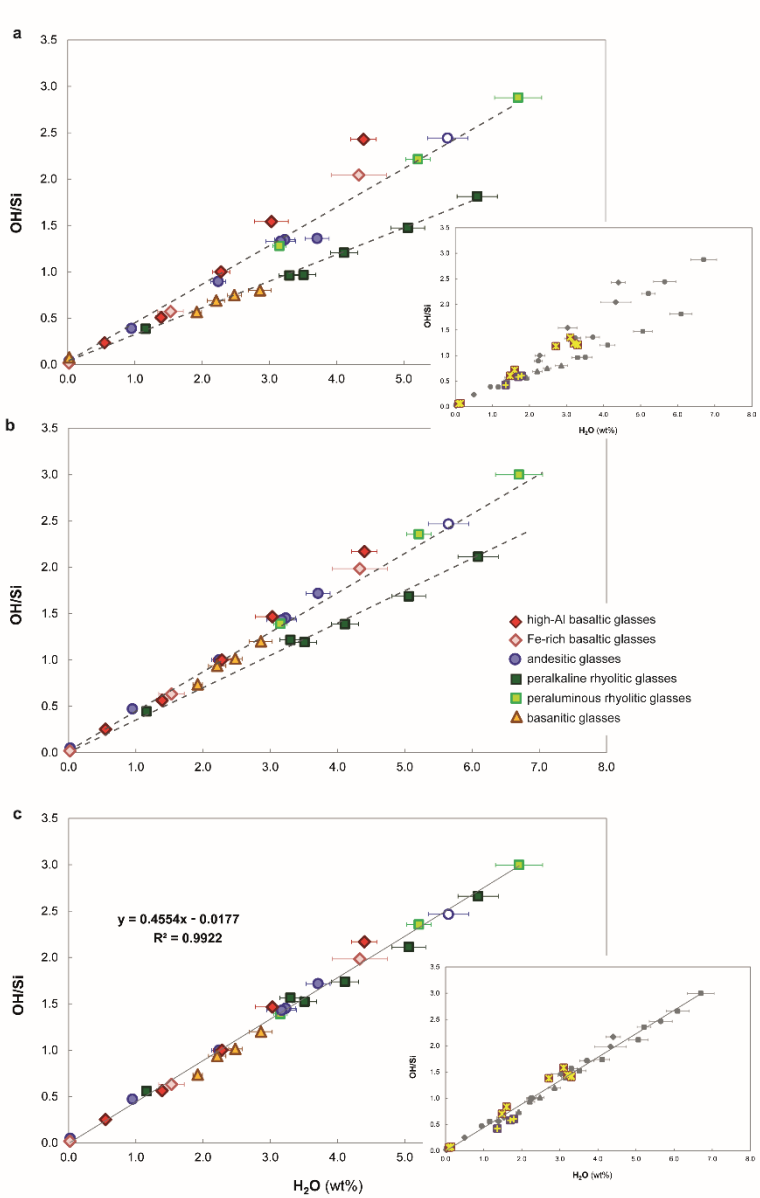

1245

1246 **Fig. 9.** a) Internal calibration diagram showing variation of the "OH/Si" ratio (i.e. the
1247 area ratio between the total water band, A_{OH}, and the total alumino-silicate band region, $A_{Al\text{-}Si}$)
1248 versus water content. b) Internal calibration lines after applying the density-related correction.
1249 c) Internal calibration line after correcting for the high Raman scattering of the 980 cm^{-1} band
1250 in peralkaline rhyolites. All samples define a single calibration line passing through the
1251 origin. The insets show the non-corrected glass inclusion compositions (symbols as in Fig. 8).
1252 Signal intensities were normalized to laser power and acquisition time, and to the areas of the
1253 82-72f#9 internal standard.

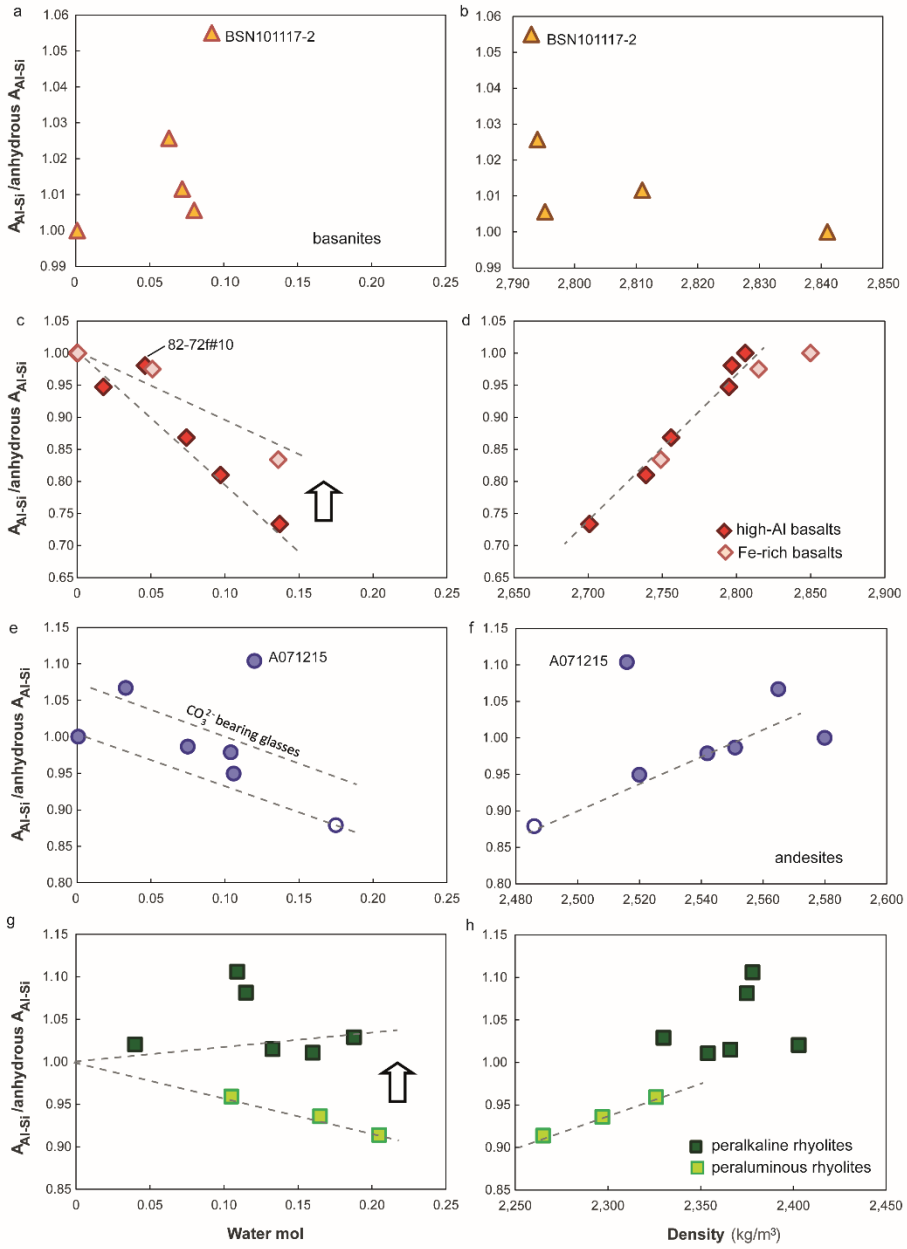

1254

1255 **Fig. 10.** Evolution of the area of the alumino-silicate band (expressed as ratio between
1256 the alumino-silicate band area of hydrous glasses and that of the anhydrous glass) with water
1257 content (left column) and density (right column) of basanitic (a-b), basaltic (c-d), andesitic (e-
1258 f) and rhyolitic (g-h) glasses. Grey dashed curves show the main trends. The arrows highlight
1259 the different behavior of Fe-rich and Fe-poor glasses with similar compositions. Microlite-
1260 bearing andesitic glass A011215 is represented by an empty blue circle.

1261

1262 **TABLES**

Table 1
Synthesis conditions and volatile composition of reference glasses.

GLASSES	Series	Starting material	Synthesis method		Capsule material	P (GPa)	T (K)	Time (h)	Loaded H_2O wt%	Analytical technique	Thickness (cm)	Density[a]	Water content			CO_2	References
												(kg m^{-3})	wt%	1σ[c]	mol	wt%	
Basanitic																	
BSN050417	Alkaline	Thueyts tephra	GMF		$Au_{80}Pd_{20}$	0	1573	4		FTIR	0.0410(5)	2841(37)	0.023	0.001	0.001		This study
BSN081117–1	Alkaline	Thueyts tephra	PC	1/2″	$Au_{80}Pd_{20}$	1.5	1598	3		FTIR	0.0054(7)	2811(21)	2.21	0.13	0.072	0.48 ± 0.07	This study
BSN081117–2	Alkaline	Thueyts tephra	PC	1/2″	$Au_{80}Pd_{20}$	1.5	1598	3		FTIR/CHNS	0.0055(7)	2794(11)	2.48	0.10	0.080	1.76 ± 0.03	This study
BSN101117–1	Alkaline	Thueyts tephra	PC	1/2″	$Au_{80}Pd_{20}$	1.5	1598	3		FTIR/CHNS	0.0095(1)	2793(43)	1.92	0.07	0.063	0.82 ± 0.03	This study
BSN101117–2	Alkaline	Thueyts tephra	PC	1/2″	$Au_{80}Pd_{20}$	2.2	1598	3		FTIR/CHNS	0.0022(3)	2790(48)	2.86	0.17	0.092	2.35 ± 0.15	This study
Basaltic																	
82-72f#22	Tholeiitic	Giant Crater Lava Field	GMF			0	1564	5.0				2806	< 0.05				[1], [2]
82-72f#19	Tholeiitic	Giant Crater Lava Field	MHC		$Au_{80}Pd_{20}$	0.01	1503	2.1		SIMS/FTIR		2795[b]	0.58	0.05	0.020		[1]
82-72f#10	Tholeiitic	Giant Crater Lava Field	MHC		$Au_{80}Pd_{20}$	0.025	1486	2.0		SIMS		2797	1.39	0.08	0.046		[1], [2]
82-72f#9	Tholeiitic	Giant Crater Lava Field	MHC		$Au_{90}Pd_{10}$	0.05	1472	2.0		SIMS		2756	2.28	0.13	0.074		[1], [2]
82-72f#7	Tholeiitic	Giant Crater Lava Field	MHC		$Au_{90}Pd_{10}$	0.10	1446	2.0		SIMS		2739	3.03	0.25	0.097		[1], [2]
82-72f#12	Tholeiitic	Giant Crater Lava Field	MHC		$Au_{90}Pd_{10}$	0.20	1443	3.1		SIMS		2701	4.40	0.16	0.137		[1], [2]
B250317	Tholeiitic	Holuhraun tephra	GMF		$Au_{80}Pd_{20}$	0	1573	3.0		FTIR	0.0250(4)	2850(33)	0.017	0.001	0.001		This study
WM23/3	Tholeiitic	Holuhraun tephra	PC	1/2″	$Au_{80}Pd_{20}$	1.0	1573	68	3.7	FTIR	0.0324(4)	2815[b]	1.53	0.19	0.051		This study
B6b	Tholeiitic	Holuhraun tephra	PC	1/2″	$Au_{80}Pd_{20}$	1.0	1473	2.0	5	FTIR	0.0016(1)	2749(11)	4.33	0.41	0.136		This study
Andesitic																	
A040417	Calcalkaline	Synthetic	GMF		$Au_{80}Pd_{20}$	0	1573	20		FTIR	0.0181(6)	2580(1)	0.024	0.003	0.001		This study
A030417	Calcalkaline	Synthetic	PC	1/2″	$Au_{80}Pd_{20}$	0.75	1573	24	1.0	FTIR	0.0120(2)	2565(4)	0.95	0.05	0.033	0.28 ± 0.02	This study
A310317	Calcalkaline	Synthetic	PC	1/2″	$Au_{80}Pd_{20}$	1.1	1573	24	2.7	FTIR/CHNS	0.0451(2)	2542(22)	3.17	0.22	0.104	0.59 ± 0.01	This study
A031215	Calcalkaline	Synthetic	PC	3/4″	$Au_{80}Pd_{20}$	1.0	1573	17	2.5	FTIR	0.0357(2)	2551(5)	2.24	0.11	0.075		This study
A131115	Calcalkaline	Synthetic	PC	3/4″	$Au_{80}Pd_{20}$	1.0	1573	18	3.5	FTIR/CHNS	0.0298(5)	2520(5)	3.23	0.15	0.106		This study
A071215	Calcalkaline	Synthetic	PC	3/4″	$Au_{80}Pd_{20}$	1.0	1573	24	4.0	FTIR	0.0521(2)	2516(9)	3.71	0.18	0.120		This study
Rhyolitic																	
NSL-N1	Peralkaline	obsidian from New Zealand	IHPV		Au		1273			FTIR		2403	1.16	0.06	0.040		[3]
NSL-N3	Peralkaline	obsidian from New Zealand	IHPV		Au		1273			FTIR		2378	3.30	0.16	0.109		[3]
NSL-N3.3	Peralkaline	obsidian from New Zealand	IHPV		Au		1273			FTIR		2375	3.51	0.18	0.115		[3]
NSL-N4b	Peralkaline	obsidian from New Zealand	IHPV		Au		1273			FTIR		2366	4.11	0.20	0.133		[3]
NSL-N5	Peralkaline	obsidian from New Zealand	IHPV		Au		1273			FTIR		2354	5.06	0.25	0.160		[3]
NSL-N6	Peralkaline	obsidian from New Zealand	IHPV		Au		1273			FTIR		2330	6.09	0.30	0.188		[3]
R041215	Peraluminous	Güney Dag obsidian	PC	3/4″	$Au_{80}Pd_{20}$	1.0	1373	64	2[d]	FTIR	0.0371(2)	2326(7)	3.15	0.10	0.105		This study
R261115	Peraluminous	Güney Dag obsidian	PC	3/4″	$Au_{80}Pd_{20}$	1.0	1373	70	4[d]	FTIR	0.0434(3)	2297(2)	5.21	0.18	0.165		This study
R201115	Peraluminous	Güney Dag obsidian	PC	3/4″	$Au_{80}Pd_{20}$	1.0	1323	63	6[d]	FTIR	0.0228(3)	2265(20)	6.70	0.35	0.205		This study
Microlites-bearing																	
A011215	Calcalkaline	Synthetic	PC	3/4″	$Au_{80}Pd_{20}$	1.0	1573	18	6	FTIR	0.0135(3)	2486(27)	5.65	0.30	0.175		This study

Notes
GMF is gas-mixing furnace; MHC is Molybdenum-Hafnium-Carbide cold-seal pressure vessel; PC is non-endloaded piston cylinder; IHPV internally heated pressure vessel.
The numbers in parentheses are 1σ standard deviations, given in terms of the last unit cited.
References: [1] Médard and Groove (2008); [2] Malfait et al. (2011); [3] Withers and Behrens (1999).
[a] The sink/float method was used to measure the density of the 82-72f series of basaltic glasses; Archimedes' method for the other glasses.
[b] Density calculated using the regression line of Fig. 2.
[c] Uncertainty resulting from error propagation in Beer-Lambert equation.
[d] In addition to ~1.39 wt% H_2O of Güney Dag obsidian starting material.

1263

1264

1265

Table 2
Major element composition of reference glasses.

GLASSES	*n*	SiO_2	TiO_2	Al_2O_3	FeO	MnO	MgO	CaO	Na_2O	K_2O	P_2O_5[a]	Total	NBO/T[b]
		wt%	wt%	wt%	wt%	wt%	wt%	wt%	wt%	wt%	wt%		
BASANITIC[a]													
BSN050417	12	45.1(2)	2.47(7)	13.64(8)	10.05(11)	0.19(4)	11.16(14)	10.09(10)	3.99(12)	1.77(8)	–	98.45	0.780
BSN081117–1	12	43.8(2)	2.40(9)	13.29(9)	9.36(9)	0.19(5)	10.65(9)	9.82(17)	3.83(9)	1.76(7)	–	95.11	0.769
BSN081117–2	12	43.5(2)	2.40(11)	13.42(8)	9.07(14)	0.18(4)	10.09(7)	9.81(11)	3.78(14)	1.75(8)	–	93.97	0.739
BSN101117–1	12	43.7(3)	2.46(7)	13.57(13)	9.19(17)	0.18(4)	10.09(13)	10.15(10)	3.94(14)	1.80(9)	–	95.05	0.749
BSN101117–2	12	42.7(3)	2.48(11)	13.58(13)	9.19(17)	0.20(6)	9.69(7)	8.77(8)	3.90(14)	1.87(5)	–	92.37	0.693
BASALTIC													
82-72f#22	15	47.6(4)	0.60(6)	18.43(14)	8.13(11)	0.16(3)	10.58(10)	11.57(9)	2.33(16)	0.08(3)	0.07(3)	99.57	0.572
82-72f#19	20	46.4(5)	0.56(6)	18.26(2)	8.41(3)	0.15(2)	10.40(2)	11.51(13)	2.20(11)	0.07(3)	0.06(2)	98.05	0.571
82-72f#10	20	46.7(3)	0.52(6)	18.14(13)	8.39(23)	0.16(3)	10.44(10)	11.41(15)	2.17(11)	0.08(3)	0.06(2)	98.08	0.570
82-72f#9	20	46.9(1)	0.54(9)	18.17(12)	7.20(13)	0.15(3)	10.43(10)	11.40(15)	2.23(14)	0.07(3)	0.06(2)	97.18	0.567
82-72f#7	20	45.8(2)	0.55(7)	17.82(10)	7.41(14)	0.15(3)	10.24(14)	11.16(12)	2.18(12)	0.08(3)	0.05(2)	95.43	0.569
82-72f#12	10	45.0(2)	0.54(7)	18.25(17)	7.10(10)	0.10(2)	10.02(9)	11.28 (9)	2.09 (9)	0.07(3)	0.05(2)	94.52	0.554
B250317	15	49.7(3)	1.87(6)	13.67(14)	11.88(25)	0.21(3)	6.72(17)	11.55(21)	2.26(24)	0.21(3)	0.21(7)	98.24	0.515
WM23/3	15	48.8(2)	1.80(9)	13.31(10)	12.00(22)	0.21(4)	6.87 (9)	11.46(22)	1.98(42)	0.20(3)	0.17(5)	96.80	0.524
B6b	12	47.3(3)	1.71(11)	12.89(10)	11.54(18)	0.19(5)	6.45(10)	11.03(17)	2.08(11)	0.20(3)	0.19(5)	93.55	0.519
ANDESITIC													
A040417	10	60.0(4)	0.75 (7)	17.00(13)	4.77(11)	0.17(3)	4.32(7)	6.82(9)	4.05(45)	1.38(5)	–	99.29	0.215
A030417	10	60.5(3)	0.67 (7)	15.53(18)	5.19(10)	0.15(3)	3.69(6)	6.79(17)	3.43(34)	1.32(5)	–	97.27	0.200
A310317	10	60.0(4)	0.69 (5)	15.57(11)	4.08(13)	0.17(3)	3.44(8)	6.50(5)	3.28(38)	1.33(7)	–	95.10	0.180
A031215	9	59.9(6)	0.72(11)	16.23(20)	4.51(22)	0.18(5)	4.03(15)	6.36(23)	3.71(15)	1.42(11)	–	97.05	0.199
A131115	8	58.5(3)	0.79(10)	16.18(15)	4.41(15)	0.15(4)	4.08(9)	6.42(9)	3.73(9)	1.46(9)	–	95.71	0.207
A071215	8	57.8(3)	0.67 (6)	15.81(13)	4.79(10)	0.16(3)	3.86(16)	6.71(13)	3.70(7)	1.39(7)	–	94.87	0.214
RHYOLITIC													
NSL-N1	12	72.3(2)	0.26(5)	10.45(4)	4.15(4)	0.07(3)	0.008(3)	0.20(1)	5.28(28)	4.45(16)	–	97.15	0.049
NSL-N3	12	72.1(2)	0.21(5)	10.25(3)	4.05(5)	0.08(4)	0.011(4)	0.19(2)	5.45(31)	4.28(16)	–	96.63	0.054
NSL-N3.3	12	70.4(3)	0.22(7)	10.25(6)	4.22(5)	0.10(3)	0.006(5)	0.19(2)	5.09(37)	4.30(21)	–	94.79	0.047
NSL-N4b	12	71.3(3)	0.22(6)	10.24(5)	3.93(8)	0.09(2)	0.010(3)	0.20(2)	5.16(39)	4.22(13)	–	95.40	0.047
NSL-N5	12	70.6(3)	0.20(3)	10.17(7)	4.05(4)	0.08(2)	0.008(7)	0.19(2)	4.55(37)	4.21(9)	–	94.02	0.034
NSL-N6[c]		70.4	0.20	9.86	3.87	0.07	0.004	0.17	5.17	4.18	–	93.91	0.051
R041215[a]	10	75.1(4)	0.04(5)	12.22(8)	0.74(10)	0.07(4)	0.03(2)	0.42(5)	4.09(14)	4.46(26)	–	97.20	0.004
R261115[a]	10	73.4(3)	0.05(5)	11.89(12)	0.74 (4)	0.08(6)	0.02(2)	0.41(6)	3.92(17)	4.24(19)	–	94.76	0.001
R201115[a]	10	72.3(4)	0.04(4)	11.69(13)	0.72 (8)	0.07(4)	0.02(2)	0.32(4)	3.82(15)	4.16(24)	–	93.12	0.000
Microlites-bearing													
A011215	11	57.7(3)	0.71(5)	15.60(14)	4.49(10)	0.14(2)	3.74(10)	6.08(13)	3.59(11)	1.38(7)	–	93.39	0.192

Notes
n is the number of measurements; the numbers in parentheses are 1σ standard deviations, given in terms of the last unit cited. All Fe is reported as FeO.
[a] The P_2O_5 content of reference glasses was only measured for basaltic compositions. The P_2O_5 content of the basanitic starting material is equal to 0.7 wt%.
[b] NBO/T (i.e., non-bridging oxygen per tetrahedrally coordinated cation) is calculated on an Fe- and H_2O-free basis, following Behrens et al. (2006).
[c] calculated based on the starting composition of the dry natural obsidian.

1266

1267

Table 3
Water quantification in glass inclusions.

Sample	Provenance	Host phase	Glass composition	2D size	H_2O wt%						% host phase correct.[d]
				(μm)	SIMS/ FTIR[a]	± 1 σ	External cal. (cubic bas.)[b]	± 1 σ[c]	External cal. (linear bas.)[b]	± 1 σ[c]	
Vaggelli-3-1[e]	Santorini	Olivine	Basalt	110 × 50	3.10	0.06	3.15	0.12	3.25	0.17	0.0
Vaggelli-4-1[e]	Santorini	Olivine	Basalt	140 × 120	3.20	0.05	3.02	0.12	3.15	0.17	0.0
Vaggelli-6-1[e]	Santorini	Olivine	Basaltic andesite	210 × 110	3.30	0.04	3.27	0.13	2.98	0.19	0.0
Vaggelli-2-1[e]	Santorini	Olivine	Andesite	130 × 80	3.30	0.10	3.33	0.13	3.10	0.19	0.5
S12-371-3[e]	Santorini	Olivine	Basalt	190 × 115	2.71	0.03	2.77	0.11	2.71	0.15	0.0
S12-43-7-1[e]	Santorini	Olivine	Basalt	255 × 135	1.48	0.01	1.55	0.06	1.29	0.08	0.0
S12-43-1-1[e]	Santorini	Olivine	Basaltic andesite	65 × 50	1.60		1.64	0.06	1.62	0.09	1.0
TAO-ol1	Lanzarote	Olivine	Basanite	62 × 52	1.70	0.05	1.74	0.07	1.53	0.10	4.0
TAO-ol20	Lanzarote	Olivine	Basanite	101 × 25	1.36	0.05	1.26	0.06	1.14	0.08	1.5
TGN-ol18	Lanzarote	Olivine	Basanite	244 × 154	1.79	0.05	1.66	0.07	1.73	0.11	0.0
FZ OL37b	FAMOUS Zone	Olivine	Basalt	75 × 70	0.093	0.003	0.127	0.007	0.105	0.007	not embedded
FZ OL39	FAMOUS Zone	Olivine	Basalt	150 × 125	0.140	0.006	0.173	0.008	0.132	0.009	not embedded

Notes
[a] Water contents measured by SIMS, except for FZ OL37b and OL39 analyzed with FTIR (Schiavi et al., 2016).
[b] Water contents estimated from the regression lines of Fig. 8 (high confocality setting).
[c] Uncertainties calculated from the errors related to the linear regression (see Eq. 1 in the text) for 95% confidence interval.
[d] Arithmetic subtraction of host phase spectrum from glass spectrum.
[e] Reference: Druitt et al., 2016

1268